Highlights

Jovian upper clouds and hazes from visible and near infrared spectroscopy using CARMENES

José Ribeiro, Pedro Machado, Santiago Pérez-Hoyos, Asier Anguiano-Arteaga, Patrick Irwin

- We performed for the first time flux calibrations of Solar System data obtained by CARMENES, paving the way for future Solar System observations with this instrument.
- We performed retrievals for 5 regions of the atmosphere of Jupiter using three competing aerosol schemes and compared the results of each.
- We found that the single vertically extended chromophore model best fits the observations.

Jovian upper clouds and hazes from visible and near infrared spectroscopy using CARMENES⋆

José Ribeiro[a,b,*], Pedro Machado[a,b], Santiago Pérez-Hoyos[c], Asier Anguiano-Arteaga[c,d] and Patrick Irwin[d]

[a]Instituto de Astrofísica e Ciências do Espaço, Universidade de Lisboa, OAL, Edifício Leste, Tapada da Ajuda, PT1349-018 Lisboa, Portugal
[b]Departamento de Física, Faculdade de Ciências, Universidade de Lisboa, Edifício C8, Campo Grande, PT1749-016 Lisboa, Portugal
[c]Dpto. Física Aplicada I, Faculty of Engineering Bilbao, Universidad del País Vasco UPV/EHU, 48013 Bilbao, Spain
[d]Department of Physics, Atmospheric, Oceanic and Planetary Physics, University of Oxford, Oxford, UK

ARTICLE INFO

Keywords:
Jupiter, atmosphere
Atmospheres, structure
Radiative transfer

ABSTRACT

The aerosol scheme for Jupiter's upper hazes and clouds is still debated to this day, for the Crème Brûlée aerosol scheme has trouble in fitting some specific Jovian atmospheric features (Braude et al., 2020; Dahl et al., 2021). We use here first-time observations of Jupiter by CARMENES in 2019, from visible to near infrared (0.52 – 1.71 μm), to test three competing aerosols schemes. These observations are unique due to their spectral coverage with both high spatial and spectral resolutions, paving the way for future observations of Solar System objects. A model with two blue wavelength attenuating hazes (chromophores) by Anguiano-Arteaga et al. (2021, 2023), a model that has a single blue attenuating haze by Braude et al. (2020) and a model where the blue attenuating haze is physically constrained in a thin layer ("Crème Brûlée model") with a more up to date parameter values from Pérez-Hoyos et al. (2020). We grouped the observations into 5 regions of the atmosphere of Jupiter and performed a Minnaert limb-darkening approximation, producing synthetic spectra at 0°and 61.45°zenith angles for each. We found that the properties of the highest aerosol layer dominate the fit to the observations, with particle size (Models A and B) and cloud base abundance (Models A and C) being the most influential parameters. We found that the extended chromophore model from Braude et al. (2020) fits the observations better than the other two models. However, none of the models fully represent the observations as none achieved a $\chi^2/N_{free} < 1$. This highlights the need for improved models that consider holistic observations that extend beyond the original wavelength range of this study, encompassing data from ultraviolet to mid-infrared, to fully explain the Jovian aerosol scheme.

1. Introduction

The study of the optical and physical properties of clouds and hazes of Jupiter is necessary to understand the phenomena that occur in its atmosphere. Condensation models (Atreya et al., 1999) predict the presence of three main cloud layers in the atmosphere of Jupiter: an aqueous-ammonia cloud that blends into a water ice cloud at higher levels, located roughly at 7 bar; a solid ammonium hydrosulphide cloud around 2.5 bar; and an ammonia ice cloud located around 0.8 bar (Irwin, 2009). Above, haze layers are formed, possibly due to the dissociation of NH_3 and PH_3 and some methane haze products coming from the stratosphere (Irwin, 2009). The hazes can be located between 200 to 300 mbar, where peak ammonia photo-dissociation occurs, with an increased probability of hazes forming at around 80 mbar, where photodissociation of phosphine reaches its maximum rate (Irwin, 2009). The main constituents of Jupiter's upper clouds are white when in chemical equilibrium, such as the ammonia ice cloud layer that is expected to be located at the upper troposphere. However, various shades of browns and reds are observed that can only be explained by the presence of disequilibrium species (West et al., 2004). These aerosol species play an important role in the radiative heat budget of the atmosphere and, as a consequence, in the dynamical processes that occur in the atmosphere of the gas giant, such as stratospheric circulation or tropospheric meteorology, especially when considering the temporal and colour variability of some storms and vortices. The correct interpretation of these phenomena also has the consequence of a better understanding of exoplanetary spectra, such as the work by Heng and Li (2021), where

⋆

*Corresponding author
jlribeiro@fc.ul.pt (J. Ribeiro)
ORCID(s): 0000-0001-6350-9566 (J. Ribeiro); 0000-0001-6757-5763 (P. Machado); 0000-0002-2587-4682 (S. Pérez-Hoyos); 0000-0002-9305-1901 (A. Anguiano-Arteaga); 0000-0002-6772-384X (P. Irwin)

they analysed phase curves of Jupiter obtained by the Cassini spacecraft as a case study for gas-giant exoplanets, or the work by Montañes-Rodriguez et al. (2015), where they analysed the ultraviolet, visible and near-infrared transmission spectrum of Jupiter, as if it were a transiting exoplanet.

The current understanding of the aerosol structure is the idealised cloud structure by Atreya et al. (1998), with a water-ammonia solution cloud with a base at 6 bar, an ammonium hydrosulfide cloud with a base at 2.2 bar and an ammonia ice cloud at 0.7 bar. However, the distribution of aerosols higher in the atmosphere remains a source of debate, particularly regarding the spatial variability, composition and origin of the blue-absorbing compounds. Direct measurements by the Galileo probe showed a different aerosol configuration than what was expected, with the ammonia ice cloud having an effective pressure of less than 440 mbar, a physically thin mid-level, putative NH_4SH cloud at a pressure of 1.2 bars and deep cloud, putative of water-ice, found much deeper, below 14 bar (Sromovsky and Fry, 2002; Niemann et al., 1996, 1998). This is likely due to the drier conditions of the region the Galileo probe entered. The only current way to retrieve the properties of the upper clouds and hazes of Jupiter is through remote sensing. While for the stratosphere of Jupiter direct inversion is possible, since multiple scattering is not relevant, for the troposphere multiple scattering plays a more important role, leading to multiple solutions to the radiative transfer equations that fit the data to within the uncertainties (West et al., 2004). Baines et al. (2019) introduced the colloquially known "Crème Brûlée" model, where these blue-absorbing aerosol particles are located in a thin layer above the deep ammonia cloud layer. This aerosol model utilises a potential universal chromophore, based on the red compound obtained in a laboratory by Carlson et al. (2016) from the reaction of photolysed ammonia with acetylene, as suggested by Sromovsky et al. (2017) based on the fits to Cassini's Visible and Infrared Mapping Spectrometer (VIMS-V) observations in the visible. The contrast in results from Sromovsky and Fry (2002) and Atreya et al. (1998) show that we still do not fully grasp the aerosol structure that is present in Jupiter and how to properly model the Jovian atmosphere. Adding to this, models usually utilise spherical aerosol particles due to their simplicity to model and parametrise, but results from Zhang et al. (2015) show that fractal aggregates may better represent stratospheric haze, raising questions on how best to represent the particles of each aerosol population.

The available Jupiter observations have their own particular constraints. For example, Hubble Space Telescope Wide Field Camera 3 (HST/WFC3) observations have high spatial resolution but suffer from low spectral resolution, the standard Jupiter Cassini/VIMS calibration suffers from pointing issues (Sromovsky et al., 2017), and observations only span 2000-2001, James Webb Space Telescope (JWST), while having provided many Jupiter observations, is limited to wavelengths larger than 0.6 μm, being unable to capture the range where the chromophore absorption is strongest, observations with the Multi Unit Spectroscopic Explorer at the Very Large Telescope (MUSE/VLT) can simultaneously capture spectra from different points of Jupiter. However, these are limited to a lower spectral resolution and a smaller spectral range. Other alternative aerosol schemes have been proposed for the Jovian atmosphere. Pérez-Hoyos et al. (2020) proposed a more extended and less blue-absorbing chromophore layer (scenario A) for a North Temperate Belt disturbance using HST observations and Braude et al. (2020) for the overall latitudinal structure through the use of (MUSE/VLT), without fully discarding the possible existence of a "universal chromophore". Anguiano-Arteaga et al. (2023, 2021) however, suggested the presence of two colouring aerosols, with one very similar to the "universal chromophore" proposed by Sromovsky et al. (2017) and a new colouring agent at the tropospheric levels, through their analysis of HST's Wide Field Camera 3 (WFC3) images of Jupiter's Great Red Spot, its surroundings and the Oval BA.

The existence of multiple, and sometimes conflicting, proposed aerosol configurations highlights the uncertainty on how the aerosols are vertically distributed, their intrinsic properties and their temporal and spatial variability. All of which could be related to the nature of the absorbing particles themselves as well as the chemistry and transport processes they are subjected to.

To further constrain the properties of the Jovian aerosol configuration, we use ground-based observations of Jupiter using the Calar Alto high-Resolution search for M dwarfs with Exoearths with Near-infrared and optical Échelle Spectrographs (CARMENES) in Calar-Alto, Spain. These spectrographs have a spectral resolution of R = 80,000 – 100,000 and combined have a spectral range of 0.52–1.71 μm. These high-resolution spectra were purposely downgraded in spectral resolution, so they can match the available methane bands' spectral resolution, in order to study the aerosols, which are expected to be smooth as a function of wavelength, allowing us to use the retrieved aerosol properties for a future higher-resolution chemical analysis. We applied the models from previous works by Braude et al. (2020); Anguiano-Arteaga et al. (2023, 2021); Pérez-Hoyos et al. (2020), performing retrievals of various atmospheric parameters and comparing the results from each to better understand the nature of the aerosols that are present in the atmosphere of Jupiter. The unique spectral coverage of CARMENES enables us to retrieve properties

of the chromophore/s that absorb in shorter wavelengths while simultaneously retrieving the physical properties of deeper aerosols that affect the spectra at longer wavelengths in the visible and the near infrared, thus allowing for a more complete characterisation of Jupiter's aerosols. Using CARMENES in this context provides an additional, independent dataset with high spectral resolution and simultaneous VIS–NIR coverage, bridging a wavelength range that is not always accessible with the same combination of resolution and simultaneous coverage in other instruments. This added, high-quality information enables us to further constrain key atmospheric parameters, such as aerosol optical properties and vertical structure, and to cross-validate retrieval results obtained from other instruments, thereby further assessing the robustness of the proposed atmospheric schemes. This dataset has the advantage of enabling future higher-resolution studies of specific spectral features due to chemical species, constraining their abundance and isotopic ratios, and is one of the highest spectral resolution spectrographs available that can observe the visible and near-infrared spectrum simultaneously, prior to the first light of the combined High Accuracy Radial velocity Planet Searcher (HARPS) and Near Infra Red Planet Searcher (NIRPS) mounted at the European Southern Observatory (ESO).

2. Data

2.1. CARMENES observations

The Calar Alto high-Resolution search for M dwarfs with Exoearths with Near-infrared and optical Échelle Spectrographs (CARMENES) is a high-resolution instrument operating at the 3.5m telescope at the Calar Alto Observatory in Spain. It consists of two separate spectrographs covering wavelength ranges of 0.52 to 0.96 μm and from 0.96 to 1.71 μm with spectral resolutions R = 80,000 – 100,000, each of which performs high-accuracy radial-velocity measurements ($\sim$1 m/s) with long-term stability (Quirrenbach et al., 2016; Nowak et al., 2020; Murgas et al., 2023).

The Jupiter observation campaign occurred on the night of the 29th of May, 2019 (data available at the Calar Alto Archive)[1]. It lasted approximately 4 and a half hours, acquiring over 150 spectra both in the VIS (0.5 – 0.9 microns) and NIR (0.9 – 1.7 microns). Spectra were obtained from the centre of the disc to close to the terminator ($\sim$ 60°Lon), from the North Tropical Zone (NTrZ) to the South Tropical Zone (STrZ), with most of them located in the Equatorial Zone (EZ). However, no Great Red Spot (GRS) spectra were obtained during this observation campaign.

For this work, we also used a previous Saturn observation campaign that occurred on the night of the 14th of June, 2017 (data available at the Calar Alto Archive) [2]. It lasted approximately 3 and a half hours, acquiring 58 spectra both in the VIS and NIR. Spectra were obtained from the northern hemisphere from the centre of the disc to close to the terminator at various latitudes. Most of the southern hemisphere was unobservable due to the shadowing of the rings at that time of the Saturnian year. In particular, we use in this work six spectra from Saturn's B ring, whose importance is explained in the next section.

2.2. Data reduction and calibration

The data were processed and wavelength-calibrated using the standard CARMENES data processing pipeline (Quirrenbach et al., 2016), resulting in a single spectrum for VIS and NIR for each acquisition. These spectra were associated with images captured with the Acquisition and Guiding Camera (AGC) of CARMENES, which were navigated with the use of the WinJUPOS program [3]. Given the resolution of the AGC images, the location of Io or Europa, whenever they were visible in the AGC images, was used to constrain the size and inclination of the grid over Jupiter to determine the coordinates of the spectrograph's FOV (Figure 1). The outcome of this navigation and image-to-spectra association is 64 pairs of VIS and NIR spectra from the STrZ to the NTrZ covering various longitudes. Table 1 shows the number of spectra considered for each region. STrZ is not shown because it only consisted of a single spectrum; therefore, no limb-darkening approximation was possible, and it was not considered.

The original purpose of this observation campaign was to study winds using the Doppler Velocimetry Method (Machado et al., 2012, 2014). For this method, no flux calibration is required to obtain wind measurements. Hence, no calibration star was observed. The publicly available star spectra from CARMENES close to the date of these observations consist only of the M dwarf type, but we found them inadequate for the flux calibration required here, due to sky transparency and brightness issues. For doing so, we used Saturn's Ring-B observations performed with CARMENES during the 13th of June 2017 Saturn observations. Six ring spectra were obtained, which were

[1] https://caha.sdc.cab.inta-csic.es/calto/jsp/searchform.jsp, CAHA_ID:297978–298301
[2] https://caha.sdc.cab.inta-csic.es/calto/jsp/searchform.jsp, CAHA_ID:259154–259269
[3] https://jupos.org

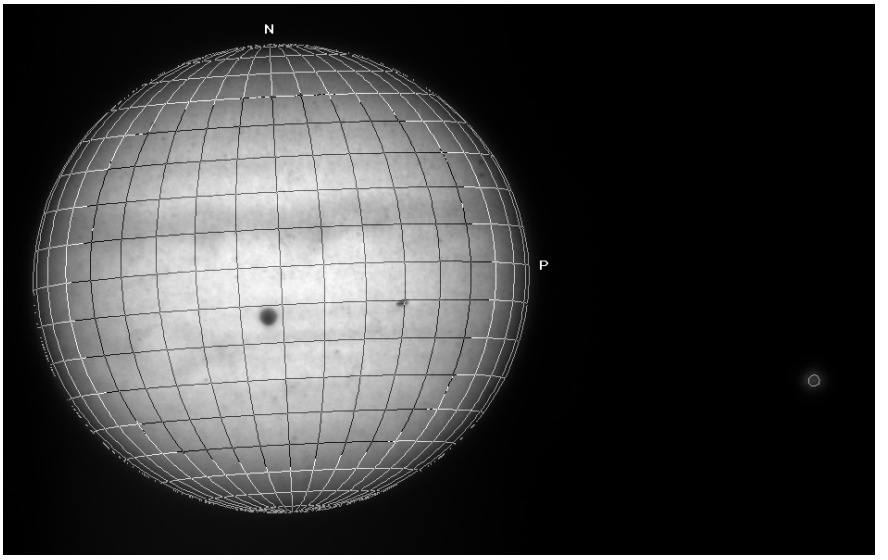

Figure 1: Navigation of a sample Acquisition and Guiding Camera (AGC) image with WinJupos. The dark circular spot is the field of view (FOV) of CARMENES over Jupiter. The grid represents 10°both in planetographic latitude and longitude. Europa's position in the sky is also highlighted (white circle on the right).

Table 1
Number of spectra considered for each of the regions in this study

Region	Number of spectra
EZ	34
NEB	13
SEB	7
SEB transition	6
NEB transition	3

downgraded through a Gaussian convolution to R = 173 – 570, approximately matching the spectral resolution of the ring spectra obtained with Cassini/VIMS (Cuzzi et al., 2009). Saturn's B-ring spectra are a reliable calibrator for they have no temporal changes, the spectra are well studied and relatively featureless or with broad clear features, hence showing a well understood spectral behaviour. We obtained the instrument response function $RF(\lambda)$ by dividing the spectrum from VIMS $F_{I/F}(\lambda)$ with our mean spectrum $F(\lambda)$ at each wavelength:

$$RF(\lambda) = \frac{F_{I/F}(\lambda)}{F(\lambda)} \tag{1}$$

We applied the response function to a centre of the disc spectrum of Saturn and compared the obtained reflectivity spectrum with results from Clark and McCord (1979) and Mendikoa et al. (2017). This comparison is shown in Figure 2, where we can see that we have an agreement of within 30 % on average for all the compared spectra. However, there are some discrepancies outside the telluric absorption wavelength ranges. We have a difference of over 70 % for both the albedo and reflectivity spectra from Mendikoa et al. (2017) around 1.2 μm and around 0.7 μm, and 0.9 μm solely for the reflectivity spectrum, likely due to changes in sky transparency. All locations of absorption bands that appear more pronounced in our Saturn spectrum. Regarding the spectrum from Clark and McCord (1979), a similar effect is observed, with the absorption bands not being as pronounced as those in our spectrum, with differences exceeding 50 %, being the bands located near 0.9 and 1.0 μm showing the highest differences, with a baseline reflectivity error of 0.16 and 0.13 at the centre of each band, respectively. The spike near 1.6 μm is not seen in both of the references and differs slightly over 60 % from the spectrum from Clark and McCord (1979), most likely due to instrumental errors. It

must be noted that some of the errors may be due to comparing observations with a lower spectral resolution than that of our data.

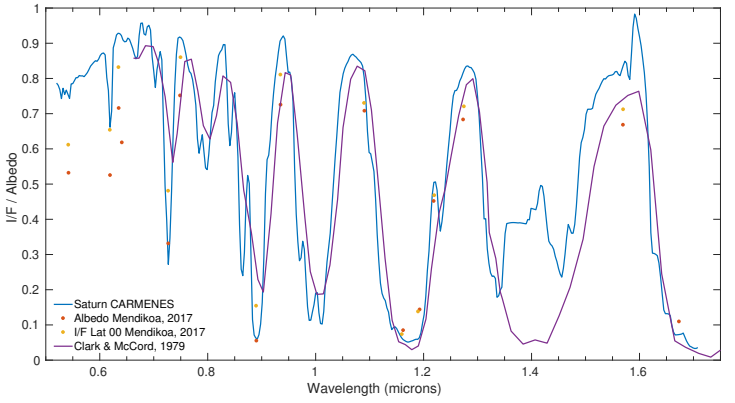

Figure 2: Comparison between a sub-observer Saturn spectrum after flux calibration with centre of disc albedo spectrum from Clark and McCord (1979) and albedo spectrum and 0°latitude spectrum from Mendikoa et al. (2017).

Lastly, we applied such a response function to a centre of the disc Jupiter spectrum. We compared our calibrated spectrum to results from Mendikoa et al. (2017) and MUSE/VLT observations of the EZ from Irwin et al. (2018) as shown in Figure 3. Our calibrated Jupiter spectrum differs on average from the MUSE data from Irwin et al. (2018) by less than 10 % with the largest discrepancy of slightly over 40 % near 0.75 μm, due to differences in spectral resolution between our data and the MUSE spectrum. While it differs on average from the spectrum of Mendikoa et al. (2017) by less than 20 % if we exclude the major discrepancy of 0.018 near 1.15 μm located in a telluric absorption wavelength region. It should be noted that this major discrepancy occurs in an absorption region of the spectrum and we are comparing very small values whose minor differences can result in significantly large relative difference values. Given this, we opted to set the *a priori* errors for our observations to be 10 % for wavelengths smaller or equal to 1 micron and 20 % for the rest and we set a baseline error of 10 $\mu W cm^{-2} sr^{-1} \mu m^{-1}$. This error is not necessarily the errors from the measurements, but an uncertainty provided to the retrieval code so it focuses the retrievals closer to the initial values of those with smaller *a priori* relative errors than those with larger relative errors.

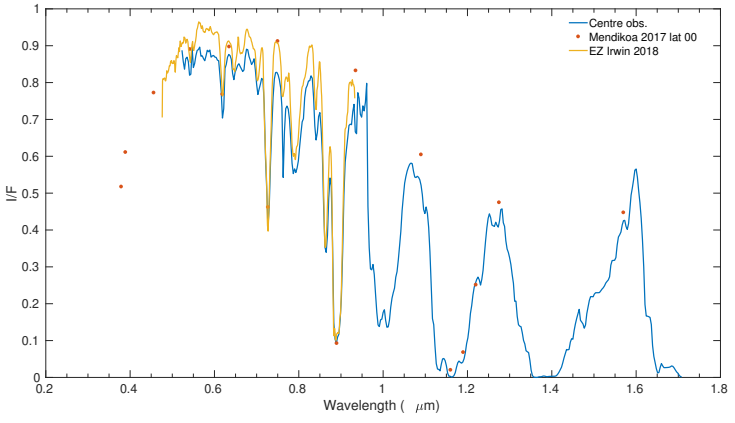

Figure 3: Comparison of Jupiter sub-observer spectra after flux calibration with reflectivity spectrum at 0°latitude from Mendikoa et al. (2017), and equatorial zone (EZ) spectrum from Irwin et al. (2018).

As shown in Figure 3, this is a reasonable flux-calibrated Jupiter spectrum when compared to other results, despite the constraints due to the initial goals of the observations. It must be noted that the spectral resolution of our spectra

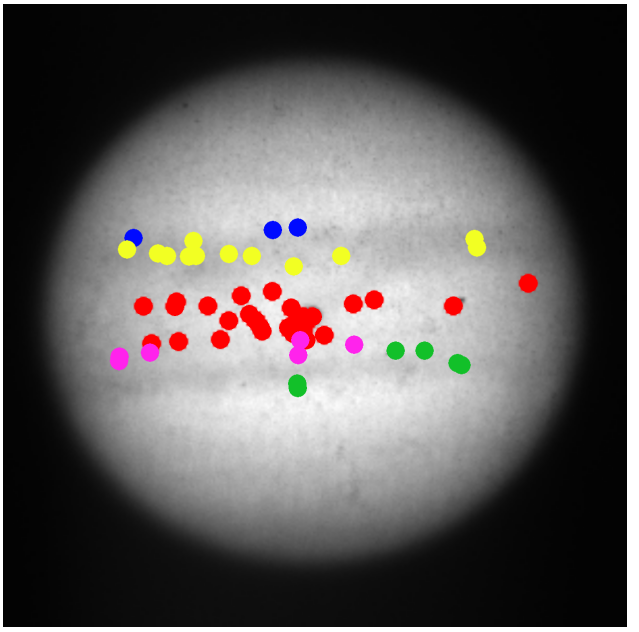

Figure 4: Location of the spectra used to perform the Minnaert limb-darkening approximation for each region considered in this study. Red for EZ, yellow for NEB, green for SEB, pink for SEB transition and blue for NEB transition. The Jupiter AGC image represented corresponds only to the spectra of the EZ whose longitude was closest to 0°.

matches that of the available spectral data of methane, the dominant gaseous source of opacity in the Jovian spectra for this wavelength range.

We used the Planetary Spectrum Generator tool (Villanueva et al., 2018) to retrieve the telluric transmittance spectrum as seen from an observatory at 2.600 m above sea level (closest option available to the altitude of the Calar Alto observatory, approximately 2.100 m). We used this spectrum to mask the ranges of our Jovian spectra that had a transmittance less than 90 % for a water vapour column of 10 % of the tropical water profile, so only higher transmittance values are considered in our retrievals. This corresponds to masking about 25 % of each spectrum. These will be indicated as grey areas in the plots in section 4.

2.3. Limb darkening behaviour

With the spectra flux calibrated, we grouped them based on which band/belt of Jupiter they were taken from. The Equatorial Zone (EZ), the South Equatorial Belt (SEB), the North Equatorial Belt (NEB) and two transition regions between belts/bands, between the EZ and SEB (SEB transition) and between the NEB and North Tropical Zone (NEB transition). Figure 4 shows the location of these spectra over the disk of Jupiter, and Table 1 shows how many observations were considered per region.

We performed a Minnaert limb-darkening approximation (Minnaert, 1941) for each region, similarly to other works on giant planets by Irwin et al. (2021, 2022); Pérez-Hoyos et al. (2020). The approximation states that the reflectivity at a particular wavelength can be approximated as:

$$\frac{I}{F} = \left(\frac{I}{F}\right)_0 \mu_0^k \mu^{k-1} \tag{2}$$

Where $(I/F)_0$ is the reflectivity at nadir viewing geometry, k is the limb-darkening parameter, μ is the cosine of the emission angle, and μ_0 is the cosine of the solar incidence angle.

We then performed a linear least-squares fit to the logarithm of Equation 2 to obtain $(I/F)_0$ and k:

$$ln\left(\mu\frac{I}{F}\right) = ln\left(\frac{I}{F}\right)_0 + kln(\mu\mu_0) \tag{3}$$

We tested three specific wavelengths (889 nm, 634 nm and 1279 nm) from the continuum to see if this approximation was reasonable. Being satisfied with the results for the Equatorial Zone region (Figure: 5), we proceeded

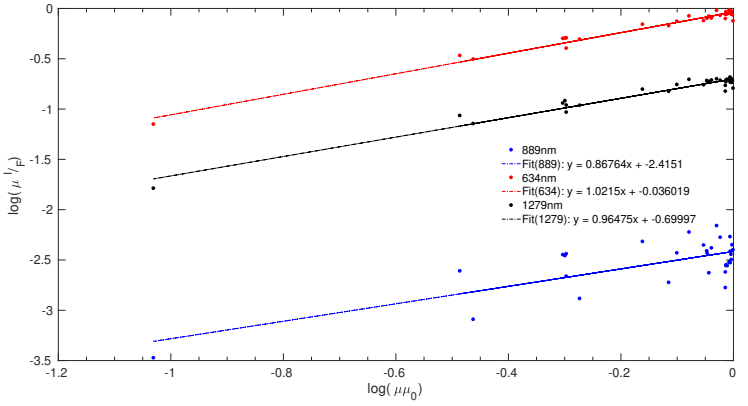

Figure 5: Sample Minnaert fits for the EZ region and three wavelengths: 889 nm in blue, 634 nm in red and 1279 nm in black.

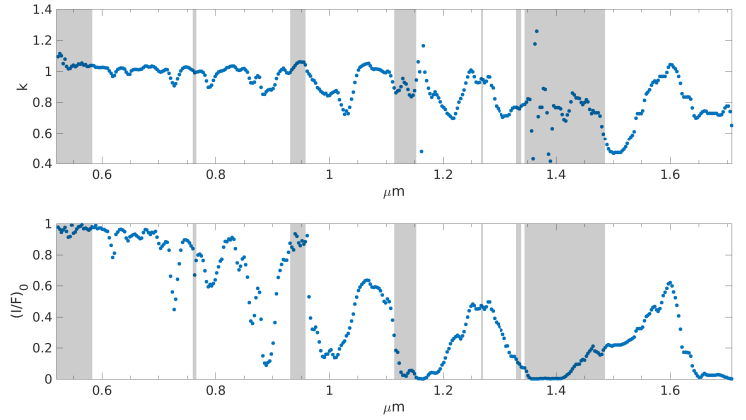

Figure 6: Retrieved limb-darkening coefficient (k) and reflectivity $(I/F)_0$ at nadir viewing geometry for the Minnaert limb-darkening approximation for the spectra of the EZ. Grey shaded areas correspond to telluric absorption.

to perform the same analysis for every wavelength (0.520 μm to 1.708 μm with a spacing of 0.003 μm) in the spectral range, obtaining the reflectivity spectrum at 0°zenith angle and the limb-darkening coefficient k (Figure: 6).

With these factors successfully calculated and using Equation 2, we produced two synthetic spectra for each of the regions to be used in the retrievals, one at 0°zenith angle and another at 61.45°zenith angle. These two angles correspond to two of the five zenith angles of the Gauss-Lobatto multiple-scattering radiative transfer model employed by NEMESIS (Irwin et al., 2008). The largest angle is such that we retrieve the limb-darkening/limb-brightening effects on the spectra without excessive computational time. The azimuth angles were calculated considering the average latitude of the observations corresponding to a specific region and the two zenith angles previously mentioned, for all five regions.

Lastly, we converted from I/F to spectral radiance ($\mu W cm^{-2} sr^{-1} \mu m^{-1}$) by applying the reference extraterrestrial solar spectrum from Chance and Kurucz (2010), accounting for the distance between Jupiter and the Sun. These are the spectra that are used across all atmospheric models in this work. From this point, these spectra obtained from this approximation method will be referred to as "Observations" throughout the rest of the document.

3. Models

We made use of the NEMESIS (Nonlinear Optimal Estimator for MultivariatE Spectral analySIS) radiative transfer suite (Irwin et al., 2008) to model the atmosphere of Jupiter. This general-purpose tool covers both reflection and emission from any planetary atmosphere in scattering and non-scattering environments. The radiative transfer calculations are performed here using the correlated-k mode with k-tables for NH_3 and $^{12}CH_4$ precomputed from HITRAN2020 line lists (Gordon et al., 2022) with k-coefficients for wavelengths less than 1 μm from Karkoschka and Tomasko (2010) for methane and from Coles et al. (2018) for ammonia.

This tool employs an optimal estimator scheme (Rodgers, 2000) to determine the most likely values of parameters that define the atmospheric model, given initial *a priori* values and uncertainties. With this, NEMESIS can retrieve the atmospheric parameters that best reproduce the observed spectral radiance as a function of wavelength simultaneously for all viewing geometries under consideration, as well as the parameter uncertainties based on how sensitive the model is to them.

To discern the quality of the fit, NEMESIS tries to minimise the mean quadratic deviation after each iteration during a retrieval:

$$\chi^2/N = \frac{1}{N}\sum_{j=1}^{N}\frac{1}{M}\sum_{i=1}^{M}\frac{(R_{ij}^{obs}-R_{ij}^{mod})^2}{(\sigma R_{ij}^{obs})^2} \tag{4}$$

Where N is the number of wavelengths for a spectrum (293), M is the number of viewing geometries (2), R_{ij}^{obs} is the spectral radiance at a certain wavelength of the spectrum being considered, R_{ij}^{mod} is the obtained spectral radiance at the same wavelength produced by the model and σR_{ij}^{obs} is the corresponding error in spectral radiance of the spectrum at the specific wavelength.

To better compare all the atmospheric models being used in this work, we use a modified version of equation 4:

$$\chi^2/N_{free} = \frac{1}{N_{free}}\sum_{j=1}^{N_{free}}\frac{1}{M}\sum_{i=1}^{M}\frac{(R_{ij}^{obs}-R_{ij}^{mod})^2}{(\sigma R_{ij}^{obs})^2} \tag{5}$$

Here we used N_{free} instead of N. N_{free} is the difference between N and the number of free parameters in the model being retrieved. The more parameters being retrieved for the same number of data points and modelled spectrum, the smaller N_{free} will be for a given model to observation difference.

3.1. Atmospheric models

We are testing three different atmospheric models using the same data: Model A from Anguiano-Arteaga et al. (2021, 2023) is a two-layer, vertically extended, chromophore model, parametrised by the cloud base height, cloud base particle abundance and fractional scale height, where the last two are read as logarithmic values so as never to be negative (see section 3.3). Model B from Braude et al. (2020) is a single, more vertical extended chromophore model, parametrised so that the specific density profile is shaped as a Gaussian by the peak specific density, the pressure level of the peak and the width of the distribution in units of log(pressure). Model C is the so-called "crème-brûlée" model from Sromovsky et al. (2017); Baines et al. (2019), with a single highly vertically concentrated chromophore layer, parametrised solely by the base pressure and number density. Here we will use the parameters retrieved from Pérez-Hoyos et al. (2020) for the crème-brûlée model (called scenario B in that paper) as the priors for model C.

Each of the original models had a slightly different atmospheric scheme. Model A covers pressure levels from 2 bar to 1 mbar, divided into 32 homogeneous layers. The temperature-pressure profile is from Seiff et al. (1998). Model B covers pressure levels from 10 bar to 1 mbar. The atmosphere is divided into 40 homogeneous layers, spaced closer together in the regions of greatest vertical sensitivity (0.1 to 2 bar) and further apart in those with less. The temperature-pressure profile results from the averaging of profiles from Fletcher et al. (2009) and extrapolated to higher pressures using a dry adiabat. Model C is similar to model A and covers pressure levels from 2 bar to 1 mbar, divided into 32 homogenous layers, and the temperature-pressure profile is from Seiff et al. (1998) as well. We decided to use the original vertical grid for each model and then discuss in section 5.2 how these different atmospheric schemes impact the retrievals performed with each model.

3.2. Gas absorption and distribution

The composition of the atmospheric gas for models A and C is according to Taylor et al. (2004). With the volume mixing ratios of H_2, He, and CH_4 being set to 0.86, 0.136 and $1.8{\times}10^{-3}$ respectively for all atmospheric layers.

In contrast, model B has a more complete gas composition of Jupiter when compared to the other two models. Besides the same species considered by models A and C, model B also includes NH_3, PH_3, C_2H_2, C_2H_4, C_2H_6, C_4H_2, GeH_4, AsH_3, CO and H_2O, but these species do not absorb in our wavelength range except for NH_3. The most absorbing gas species are NH_3 and CH_4 according to Braude et al. (2020). The deep volume mixing ratios for H_2, He and CH_4 were respectively set to 0.86, 0.134 and $1.8{\times}10^{-3}$ (Niemann et al., 1998; von Zahn et al., 1998) and the ammonia profile is based on the one from Fletcher et al. (2009), a "knee" profile with the "knee" pressure level at 0.6 atm. This profile is represented by a constant deep value up to the "knee" pressure level, where above the profile decreases according to a fractional scale height. The ammonia profile is limited to not exceed the saturated vapour pressure, with a relative humidity of 1.

All three models take into account the collision-induced absorption (CIA) of H_2-He and H_2-H_2 around 810 – 830 nm. These are modelled according to Borysow and Frommhold (1989) and Borysow et al. (2000) respectively.

3.3. Aerosol models

The description of the aerosols is the main focus of this work. We aim to best characterise the aerosols present in the atmosphere of Jupiter across various latitudes/regions, exploiting the unique characteristics of the CARMENES spectra. The three models share a number of characteristics. They all have three aerosol species being considered. All three models assume that the particles can be approximated as spherical Mie scatterers, and then the resulting Mie phase functions can be approximated using a double Henyey-Greenstein phase function (Henyey and Greenstein, 1941).

Model A considers a population of two blue absorbing chromophores, one located close to the tropopause and the other a few scale heights below. However, the deep cloud layer abundance is so low that this is effectively a two-aerosol-layer model. The particle size variance for all aerosol species is set to 0.1 (Pérez-Hoyos et al., 2020), the real refractive index at $\lambda = 900$ nm is 1.65 (Zhang et al., 2013) for the stratospheric haze and 1.43 (Pérez-Hoyos et al., 2020) for the tropospheric haze and the mean particle size for the tropospheric cloud is set to 5 microns (Pérez-Hoyos et al., 2020). In this study we retrieved the cloud base altitude (H_{bot}) and converted it to cloud base pressure (P_{bot}), cloud base abundance (particles/g) (N_{peak}), the fractional scale height (fsh, aerosol scale height relative to gas scale height), the mean particle radius (r), the imaginary refractive index (IRI) as a function of wavelength $k(\lambda)$ and the scaling factor of the deep cloud's *a priori* profile (S). The *a priori* parameters considered for this model were obtained from retrievals for analogous regions from the observations referred to as "Wong 2016" in the original works (Anguiano-Arteaga et al., 2023, 2021), and available in the supplementary document S1 as indicated in Anguiano-Arteaga et al. (2023). For this work, we considered the parameters corresponding to Region 5, as indicated in the original works. This corresponds to a calm region of the STrZ, away from the GRS and the Oval BA. For this model, 23 free parameters are considered per retrieval, or 563 degrees of freedom, and the *a priori* values can be seen in Table 2.

Model B considers a haze layer of small conservatively-scattering particles, an intermediate layer of chromophore particles, which are assumed to be responsible for all the blue absorption seen on Jupiter, and a thick tropospheric cloud layer of large conservatively-scattering particles at the bottom. Both the deep cloud and haze layers are modelled as continuous abundance profiles (i.e. one parameter per atmospheric level), with the deep cloud profile being considered for the lower half of the atmosphere, consisting of 8 layers, for pressure levels higher than 0.15 atm, and the haze profile the upper half, consisting of 5 layers, for lower pressure levels. The chromophore layer is modelled using a Gaussian vertical profile. The real refractive index at $\lambda = 700$ nm is set to 1.42 for the haze and the deep cloud, and at $\lambda = 600$ nm is set to 1.4 for the chromophore. The log-pressure width for the chromophore profile is set to 0.25, and the variance of the particle size for the deep cloud is set to 0.1. The parameters being retrieved with this model are the mean particle radius r, the particle size variance σ, the imaginary refractive index as a function of wavelength $k(\lambda)$, the peak specific density (particles/g) ρ_{max}, the pressure level of centre of Gaussian $P(\rho_{max})$, the volume mixing ratio (VMR) at the reference pressure level and deeper(nh_3v), the fractional scale height (fsh) above the reference pressure level and the haze and deep cloud vertical profiles. The initial parameters of the three particle populations were selected according to the values found in the literature at the time of publication of the article by Braude et al. (2020) (Stoll, 1980; Ragent et al., 1998; West et al., 2004; McLean et al., 2017), with the real refractive index of both the haze and deep cloud corresponding to ammonia ice (Martonchik et al., 1984). The *a priori* parameters considered in this work, however, are the retrieved parameters of the representative data for the EZ from Braude et al. (2020) that followed the

limb-darkening analysis of the NEB performed in the original work. We note that we leave r and σ of both the haze and chromophore, as well as $k(\lambda)$ of the chromophore, as free parameters for our retrievals, since we are also considering limb-darkening effects. In the original work, these parameters are fixed when analysing the representative data, for they were constrained by a prior limb-darkening analysis of the NEB with the goal of studying the longitudinal variability of the deep cloud layer. However, σ is fixed in the original work for both aerosols in the NEB limb-darkening analysis and EZ representative data analysis. For this model, 35 free parameters are considered per retrieval, or 551 degrees of freedom, and the *a priori* values can be seen in Table 2.

Lastly, model C is the "Crème Brûlée" aerosol model from Sromovsky et al. (2017) and Baines et al. (2019), using the priors from Pérez-Hoyos et al. (2020) (scenario B). These are more up-to-date parameters for observations closer in time to the ones used in this study and take into account the limb-darkening effect on the modelling of the aerosols. The fractional scale height of the tropospheric cloud is set to 1.0, the haze base pressure is set to 0.04 atm, the particle size variance for all aerosol species is set to 0.1, the real refractive index at $\lambda = 600$ nm for all aerosol species is set to 1.40 (Carlson et al., 2016; Martonchik et al., 1984), and the haze particle size is set to 0.1 μm. The parameters being retrieved are the cloud base pressure P_{bot}, the cloud base abundance (particles/g) N_{peak} and the mean particle radius in r. Unlike the original model in Pérez-Hoyos et al. (2020), P_{bot} and r of the stratospheric haze are set as fixed parameters, for our study does not analyse observations at higher latitudes ($> 30°$) where P_{bot} is located at lower pressure levels and r was found to be almost constant with latitude according to the authors, minimizing the number of free parameters. In total, only 7 free parameters are considered per retrieval, or 579 degrees of freedom and the *a priori* values can be seen in Table 2.

We opted to keep the original names given to each of the aerosol species of each Jovian model throughout this study. This facilitates comparison with the original results from the publications the models are from. However, it can be difficult to interpret and compare at first glance. Table 2 shows a comparison of the *a priori* parameters of each species that are being retrieved. For ease of visualisation of how each of the models compares to each other, Figure 7 shows an artistic representation of all three models and the aerosols considered by each of them.

Table 2: Table comparing all *a priori* parameters being retrieved, keeping similar aerosol species at the same level across the models

Model A				Model B			Model C		
Haze				Haze	r (μm)	0.52 ± 0.5	Stratospheric haze	N_{peak} (particles/g)	0.2 ± 0.1
					σ	0.050 ± 0.005			
Chromophore	Stratospheric haze	P_{bot} (atm)	$0.1^{+5.0}_{-0.1}$	Chromophore	ρ_{max} ($\times 10^{-4}$) (particles/g)	5.5 ± 0.7	Chromophore	N_{peak} (particles/g)	0.2 ± 0.1
		N_{peak} (particles/g)	0.57 ± 1.0						
		fsh	0.09 ± 0.1		$P(\rho_{max})$ (atm)	0.28 ± 0.03		P_{bot} (atm)	0.2 ± 0.1
		r (μm)	0.32 ± 0.03						
	Tropospheric haze	P_{bot} (atm)	$0.5^{+0.3}_{-0.2}$		r (μm)	0.050 ± 0.005		r (μm)	0.18 ± 0.018
		N_{peak} (particles/g)	52.5 ± 100						
		fsh	0.27 ± 0.10		σ	0.1 ± 0.01			
		r (μm)	0.7 ± 0.1						
Cloud	Tropospheric cloud	S ($\times 10^{-3}$)	0.93 ± 9.33	Deep cloud	r (μm)	4.40 ± 0.05	Tropospheric cloud	P_{bot} (atm)	1.5 ± 1.25
								N_{peak} (particles/g)	20.0 ± 10.0
								r (μm)	1.0 ± 0.2

The most sensitive regions for each aerosol type, across all models considered here, are the peaks of the absorption bands, depending on the particle size. The sensitivity decreases with wavelength for small particles, while it is constant for larger particles. The continuum in the visible wavelength range is governed by the main reflective layer (usually the one at the tropospheric level) and its refractive index.

4. Results

4.1. Model A

In Figure 8 we show our obtained synthetic spectra for the EZ as well as the errors and differences between observations and the obtained synthetic spectra. The fit of the limb geometry is slightly better than the nadir geometry, the synthetic spectrum converges better to the observations, and the differences are smaller. The largest differences observed between the observations and the synthetic spectra in both geometries are around the telluric absorption near 0.95 μm, perhaps due to contamination from telluric absorption when downgrading the spectral resolution. Large differences that exceed the *a priori* errors are also seen in the nadir spectra between 0.8 μm and 0.85 μm continuum and between 1.5 μm and 1.55 μm. The fits for the other regions can be seen in A.1. For all the other regions, similar

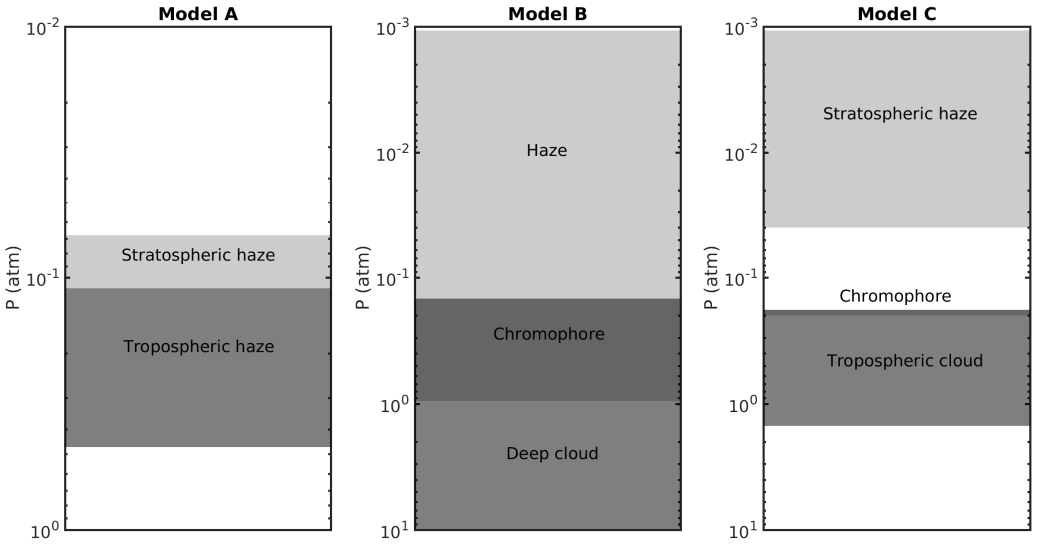

Figure 7: Representation of the three models' aerosol structure. Model A's lighter grey region is the stratospheric haze, and the darker grey one is the tropospheric haze. Model B's lighter grey region corresponds to the haze, the slightly darker grey one is the deep cloud, and the darkest region is the chromophore. The chromophore layer is within the deep cloud layer. Please note that this model (referring to model B) aerosol profiles are continuously defined at each atmospheric level (see Figure 17) and hence will be considered as more extended than the others. Model C's stratospheric haze corresponds to the light grey region, the chromophore is the thin darkest grey region on top of the deep cloud layer that is slightly lighter.

differences are found at the same wavelength intervals, and the fit for the limb viewing geometry is better than the nadir, except for the NEB region. Both the SEB and SEB transition overestimate the effect of the blue absorption around 0.6 μm, in particular for the nadir geometry. The discrepancies found at these specific wavelengths are a consequence of the limitations of the model, being unable to fully produce synthetic spectra that converge towards all the spectral features present in the observed spectra.

In Table 3, we show all parameters that were retrieved for model A, their *a priori* values and the retrieved results for each of the considered regions. We also show the resulting χ^2/N_{free} for each of the regions. The worst fitting region is the SEB, while the best is the EZ. However, the results from the SEB transition are those that deviate the most from the priors. Across all regions, the mean particle size (r) for the tropospheric haze is one order of magnitude smaller than the prior and smaller than the mean particle size (r) of the stratospheric haze. This contradicts our understanding of how larger and heavier particles should be located deeper than smaller and lighter ones. The improvement factor (Irwin et al., 2015) shows which parameters are more significant in the retrievals, with the factor closer to 1 implying a substantial reduction in the uncertainty of that parameter. Table 4 shows the calculated improvement factors for each free parameter, except for the imaginary refractive index spectra, for all regions. For all regions, the cloud base abundance (N_{peak}) of both haze species is the most significant parameter in the retrievals, with the mean particle size (r) of the stratospheric haze having an important contribution as well. The cloud base pressure (P_{bot}) of the stratospheric haze plays a more important role when considering the reddest regions (NEB, SEB and NEB transition) in this study. The importance of the fractional scale height (fsh) of the stratospheric haze, the cloud base pressure (P_{bot}) of the tropospheric haze, and the scaling factor (S) of the deep cloud profile is negligible to the retrievals. Likewise, the mean particle size (r) of the tropospheric haze does not contribute much except for the SEB transition, where the error was at least one order of magnitude smaller in comparison.

Table 3: Table of retrieved parameters using model A.

Layer	Parameter	*A priori*	EZ	NEB	SEB	SEB transition	NEB transition

Stratospheric haze	P_{bot} (atm)	$0.1^{+5.0}_{-0.1}$	$0.06^{+4.14}_{-0.06}$	$0.113^{+0.009}_{-0.009}$	$0.108^{+0.007}_{-0.007}$	$0.06^{+4.12}_{-0.06}$	$0.100^{+0.004}_{-0.005}$
	N_{peak} (particles/g)	0.57 ± 1.0	0.66 ± 0.05	0.73 ± 0.09	0.70 ± 0.09	0.31 ± 0.03	0.73 ± 0.06
	fsh	0.09 ± 0.1	0.09 ± 0.1	0.14 ± 0.15	0.06 ± 0.06	0.08 ± 0.09	0.06 ± 0.07
	r (μm)	0.32 ± 0.03	0.409 ± 0.008	0.483 ± 0.008	0.36 ± 0.01	0.51 ± 0.01	0.375 ± 0.008
	$k(\lambda)$	Figure 9					
Tropospheric haze	P_{bot} (atm)	$0.5^{+0.3}_{-0.2}$	$0.5^{+0.3}_{-0.2}$	$0.5^{+0.3}_{-0.2}$	$0.5^{+0.3}_{-0.2}$	$0.5^{+0.3}_{-0.2}$	
	N_{peak} (particles/g)	52.5 ± 100	2.8 ± 0.1	1.4 ± 0.1	1.35 ± 0.06	2.3 ± 0.1	1.6 ± 0.1
	fsh	0.27 ± 0.10	0.24 ± 0.04	0.20 ± 0.06	0.27 ± 0.05	0.14 ± 0.04	0.5 ± 0.1
	r (μm)	0.7 ± 0.1	0.086 ± 0.009	0.093 ± 0.009	0.050 ± 0.007	0.0234 ± 0.0005	0.08 ± 0.01
	$k(\lambda)$	Figure 9					
Tropospheric cloud	S ($\times 10^{-3}$)	0.93 ± 9.33	0.77 ± 7.71	0.63 ± 6.29	0.33 ± 3.34	0.58 ± 5.76	0.66 ± 6.62
Goodness of fit	χ^2/N_{free}		2.04	2.56	4.97	3.64	3.82

Table 4: Table of improvement factors of retrieved parameters using model A.

Layer	Parameter	EZ	NEB	SEB	SEB transition	NEB transition
Stratospheric haze	P_{bot}	0.20	0.99	0.99	0.20	0.99
	N_{peak}	0.96	0.93	0.93	0.95	0.95
	fsh	0.02	0.03	0	0.02	0
	r	0.81	0.84	0.70	0.77	0.80
Tropospheric haze	P_{bot}	0	0	0	0	0
	N_{peak}	0.98	0.96	0.98	0.97	0.97
	fsh	0.51	0.20	0.52	0.31	0.26
	r	0.30	0.32	0.09	0.87	0.08
Tropospheric cloud	S	0	0	0	0	0

In figure 9 we compare the *a priori* imaginary refractive index spectra for the stratospheric haze and tropospheric haze with the ones obtained from the retrieval of each of the regions considered in this study. For the stratospheric haze, we see a lot of variability from region to region, but for the tropospheric haze, the indices concentrate around 1 $\times 10^{-4}$. We see an overall increase in the attenuation at 0.5 μm relative to the prior, especially for the SEB transition. The improvement factors obtained for the imaginary refractive index spectra shown in Figure 10 demonstrate that the model is not very sensitive to the tropospheric haze across all regions, with the SEB transition being the most sensitive of the regions. For the stratospheric haze, we see that for all regions the model is very sensitive from 0.5 to 0.6 μm, showing an increased sensitivity to the imaginary refractive index at 0.5 μm for the NEB, SEB and SEB transition regions. An unusual attenuation is observed for the SEB transition and more strongly for the NEB regions centred at 1.5 μm extending from 1.0 to 1.6 μm. The model for these regions requires this feature, which is most likely an artefact, to achieve a good fit.

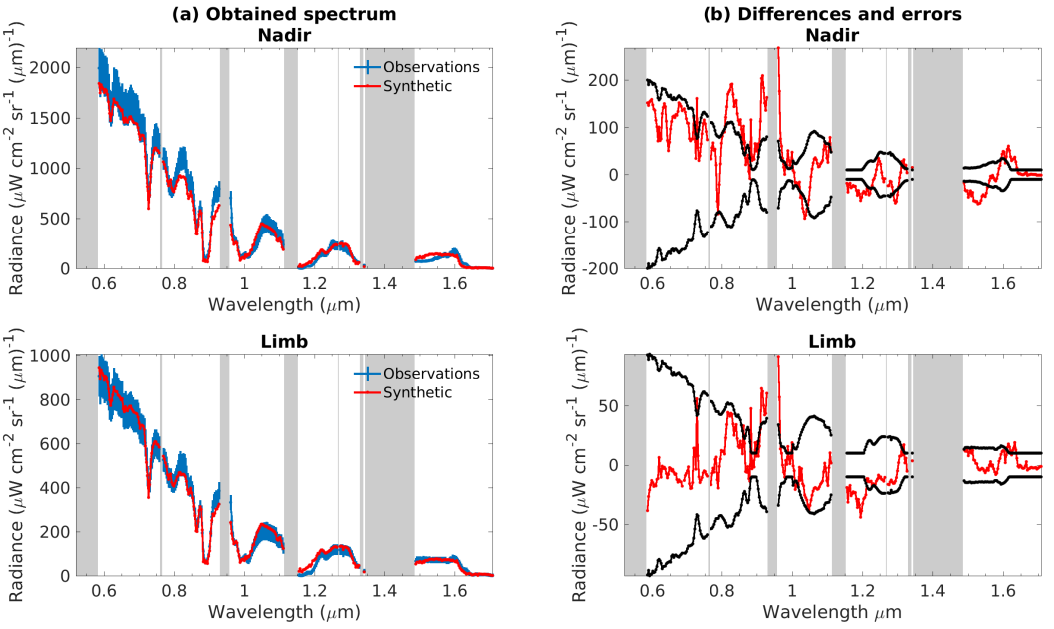

Figure 8: Comparison between observed (blue) and modelled (red) spectra (left column) and comparison between differences (red) and *a priori* errors (black) (right column) for the EZ using model A, with the grey shaded areas corresponding to telluric absorption. The top row corresponds to nadir (incidence and emission angle = 0°) and the bottom row to limb (incidence and emission angle = 61.45°).

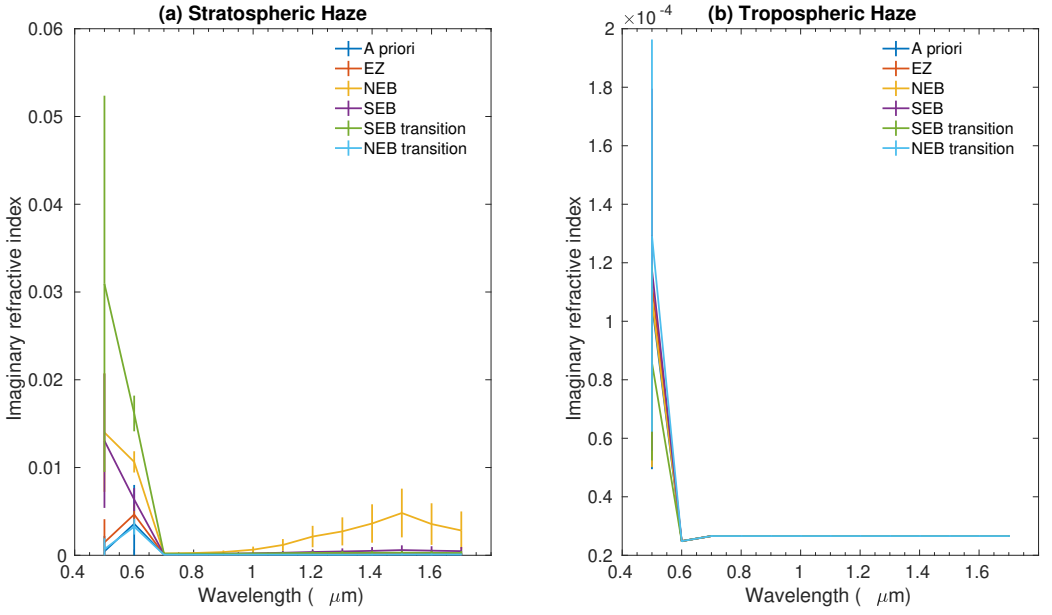

Figure 9: Imaginary refractive index spectra for the stratospheric haze and tropospheric haze, comparing the *a priori* spectrum with the retrieved spectra from all regions for model A.

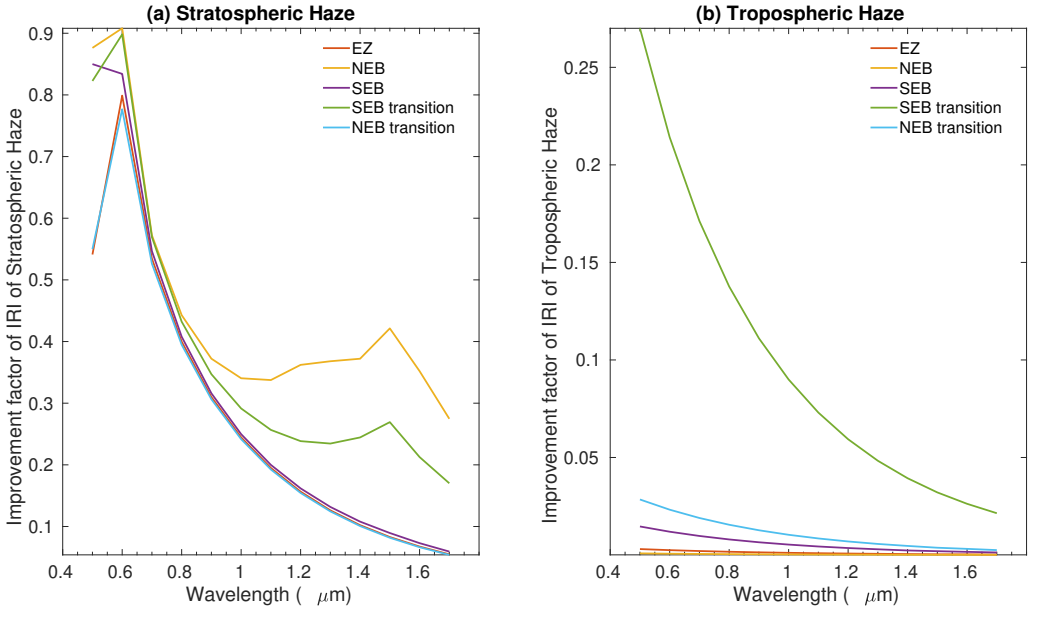

Figure 10: Imaginary refractive index spectra improvement factor for the stratospheric haze and tropospheric haze, comparing the results of each region.

4.2. Model B

In Figure 11 we show our obtained synthetic spectra for the EZ as well as the errors and differences between observations and the model. Both obtained synthetic spectra follow the observation spectra closely, with the major differences located at the same wavelengths as in model A. We note that there is a small increase in radiance at 1 μm in both the synthetic spectra that is not observed in the observations. This model also shows some trouble in fitting the shape of the spectrum of the limb beyond 1.5 μm. The fits for other regions can be found in A.2, where similar phenomena are observed. For the SEB, the model has trouble fitting the nadir observation and underestimates the radiance up to 1 μm

In Table 5, we show all parameters that were retrieved for Model B, their values and the resulting final values for each of the considered regions. We also show the resulting χ^2/N_{free} for each of the regions. The worst fitting region is the SEB, while the best is the EZ. Overall, all the retrieved parameters are within the *a priori* errors with a few exceptions. We obtained a haze mean particle size that is larger across all retrievals, for the SEB regions we retrieved a smaller particle size variance for the haze, for the chromophore the pressure level of the peak density is located at a lower level than the *a priori* estimate, the mean particle size is smaller, the deep cloud mean particle size is slightly larger and for the ammonia gas the VMR below the "knee" pressure level is larger. Table 6 shows the calculated improvement factors of the free parameters, except for the chromophore imaginary refractive index spectrum, for all regions. The most significant parameter for these retrievals using this model is the haze mean particle size. Other parameters shown in Table 6 have little to no significance for the retrievals using this model. The peak density of the chromophore's Gaussian vertical profile and peak pressure levels still have a small contribution, but the remaining free parameters shown in Table 6 have a negligible contribution to the fit.

Table 5: Table of retrieved parameters using Model B.

Layer	Parameter	*A priori*	EZ	NEB	SEB	SEB transition	NEB transition
Haze	r (μm)	0.52 ± 0.5	0.79 ± 0.02	0.71 ± 0.03	0.65 ± 0.02	0.77 ± 0.03	0.69 ± 0.02
	σ	0.050 ± 0.005	0.043 ± 0.004	0.040 ± 0.004	0.038 ± 0.004	0.044 ± 0.004	0.040 ± 0.004
Chromophore	ρ_{max} ($\times 10^{-4}$) (particles/g)	5.5 ± 0.7	5.2 ± 0.6	5.1 ± 0.6	5.4 ± 0.6	4.9 ± 0.6	5.2 ± 0.6
	$P(\rho_{max})$ (atm)	0.28 ± 0.03	0.23 ± 0.03	0.24 ± 0.03	0.19 ± 0.02	0.22 ± 0.02	0.23 ± 0.02
	r (μm)	0.050 ± 0.005	0.044 ± 0.004	0.046 ± 0.005	0.038 ± 0.004	0.045 ± 0.004	0.042 ± 0.004

	σ	0.1 ± 0.01	0.1 ± 0.01	0.1 ± 0.01	0.1 ± 0.01	0.1 ± 0.01	0.1 ± 0.01
	$k(\lambda)$	Figure 12					
Deep cloud	$r\ (\mu m)$	4.40 ± 0.05	4.45 ± 0.05	4.40 ± 0.05	4.51 ± 0.05	4.41 ± 0.05	4.46 ± 0.05
Ammonia gas	$nh_3v\ (\times 10^{-5})$	2.2 ± 0.3	1.8 ± 0.2	1.9 ± 0.2	3.0 ± 0.3	2.3 ± 0.2	2.2 ± 0.2
	fsh	0.30 ± 0.01	0.28 ± 0.01	0.280 ± 0.009	0.31 ± 0.01	0.277 ± 0.009	0.30 ± 0.01
Goodness of fit	χ^2/N_{free}		1.81	2.32	3.26	2.13	2.30

Table 6: Table of the improvement factor of free parameters using Model B.

Layer	Parameter	EZ	NEB	SEB	SEB transition	NEB transition
Haze	r	0.73	0.64	0.73	0.67	0.68
	σ	0.01	0.01	0.01	0.01	0.01
Chromophore	ρ_{max}	0.10	0.11	0.06	0.11	0.09
	$P(\rho_{max})$	0.07	0.09	0.06	0.08	0.08
	r	0.01	0.02	0.01	0.01	0.01
	σ	0	0	0	0	0
Deep cloud	r	0.01	0.02	0.01	0.02	0.01
Ammonia gas	nh_3v	0.23	0.28	0.30	0.27	0.27
	fsh	0.12	0.16	0.13	0.16	0.13

In figure 12 we compare the *a priori* imaginary refractive index spectra for the chromophore with the ones obtained from the retrieval of each of the regions considered in this study. For all regions, the imaginary refractive index spectra follow very closely the *a priori* spectrum, with a slight increase in attenuation from 1.02 μm to 1.42 μm when compared to the prior spectrum. The calculated improvement factor present in Figure 13 shows that the model is not sensitive to imaginary refractive index spectra for the chromophore for all the regions. We see an increase in sensitivity at 0.62 μm and 0.92 μm, with the EZ being more sensitive to the former and the NEB transition to the latter. However, this increase is not very significant.

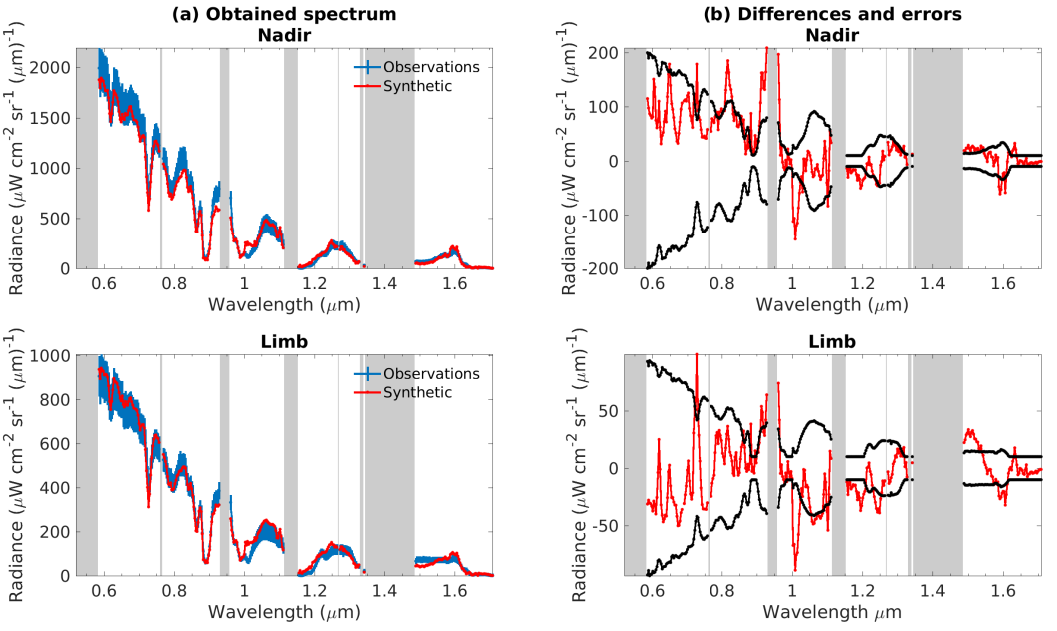

Figure 11: Comparison between observed (blue) and modelled (red) spectra (left column) and comparison between differences (red) and *a priori* errors (black) (right column) for the EZ using Model B, with the grey shaded areas corresponding to telluric absorption. The top row corresponds to nadir (incidence and emission angle = 0°) and the bottom row to limb (incidence and emission angle = 61.45°).

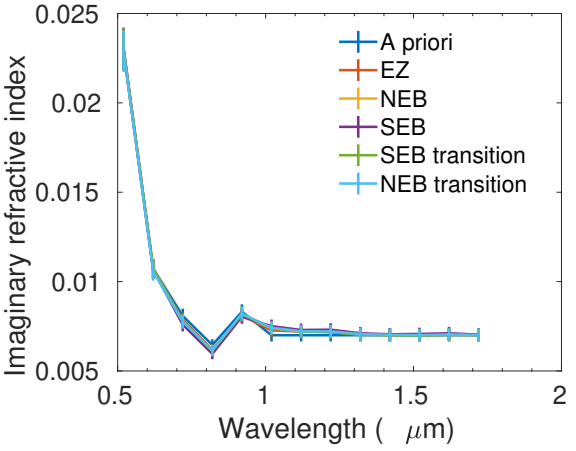

Figure 12: Imaginary refractive index spectrum for the chromophore, comparing the *a priori* spectrum with the retrieved spectra from all regions for the model from Braude et al. (2020).

4.3. Model C

Lastly, for model C, we also compare our obtained synthetic spectra for the EZ with the errors and differences between the observations and the synthetic spectra (Figure 14). The synthetic spectra of both viewing geometries are underestimated in comparison to the observation spectra up to 1 μm, the largest differences are found in similar regions to those found in the results from model A and model B, including the increase in radiance at 1 μm found in the fit of model B. There is an excess of blue absorption at smaller wavelengths in both spectra. In A.3, the fits for the remaining regions are shown. Model C has trouble fitting both viewing geometries simultaneously; either the nadir is fit better at

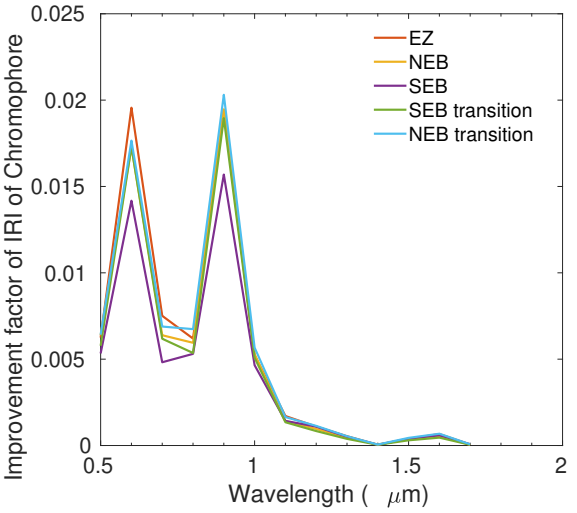

Figure 13: Imaginary refractive index spectrum improvement factor of the chromophore, comparing the results of each region.

the cost of the limb fitting, such is the case for the NEB, SEB transition and NEB transition regions, or the opposite occurs, such as in the SEB regions.

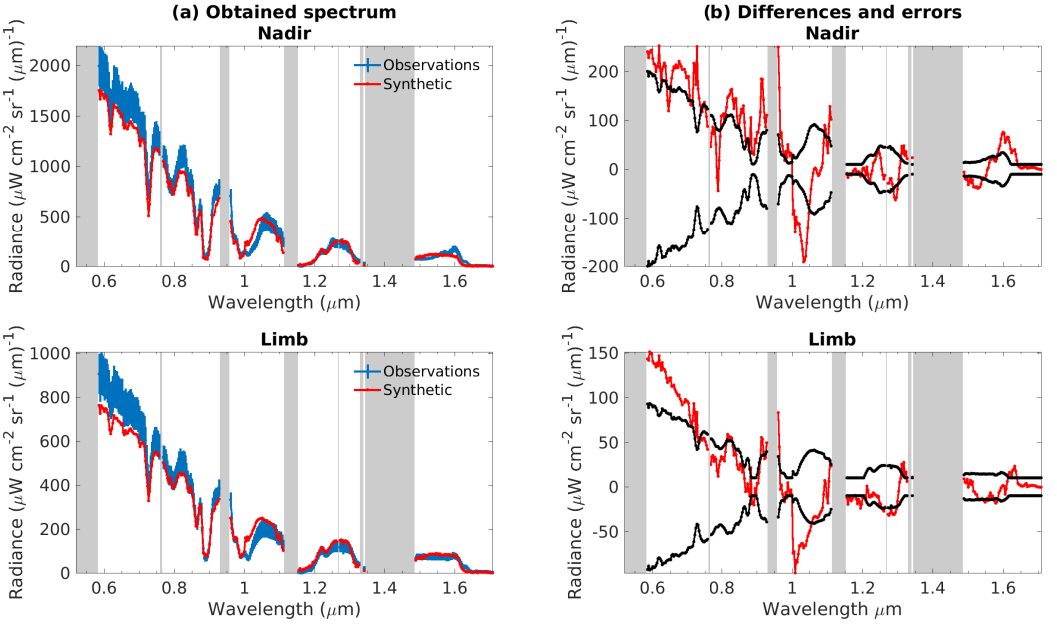

Figure 14: Comparison between observed (blue) and modelled (red) spectra (left column) and comparison between differences (red) and *a priori* errors (black) (right column) for the EZ using model C, with the grey shaded areas corresponding to telluric absorption. The top row corresponds to nadir (incidence and emission angle = 0°) and the bottom row to limb (incidence and emission angle = 61.45°).

In Table 7, we show all parameters that were retrieved for model C, their values and the resulting final values for each of the considered regions. We also show the resulting χ^2/N_{free} for each of the regions. The region with the best fit is the EZ, while the worst fit is for the SEB. All retrieved stratospheric peak density values fall within the *a priori* value

range, the base pressure level of the chromophore layer is found deeper for the NEB, SEB and NEB transition regions, the chromophore particle size is close to the prior value for all regions, the base pressure level of the tropospheric cloud is within the *a priori* value range except for the SEB transition where it is located much deeper, the base level opacity of the tropospheric cloud is lower for all regions, with the EZ being the only region whose value is within the *a priori* value range, and the mean particle size of the tropospheric cloud is one order of magnitude smaller than the expected *a priori* value, being even smaller than the chromophore mean particle size in the NEB transition and the SEB transition the mean particle size is an order of magnitude smaller than the mean particle size of the chromophore. Table 8 shows the calculated improvement factors of all the free parameters for all regions. For all regions, the cloud base pressure (P_{bot}) level and base abundance of the tropospheric cloud are the most significant parameters, followed by the cloud base abundance (N_{peak}) of the stratospheric haze. The cloud base abundance (N_{peak}) of the chromophore is more significant for all the regions, but plays a less impactful role for the EZ. The tropospheric cloud mean particle size is also relevant in the retrievals, but with less significance for the SEB transition. Lastly, the chromophore mean particle size plays a non-significant role in the retrievals across all regions.

Table 7: Table of retrieved parameters using model C.

Layer	Parameter	*A priori*	EZ	NEB	SEB	SEB transition	NEB transition
Stratospheric haze	N_{peak} (particles/g)	0.2 ± 0.1	0.17 ± 0.02	0.206 ± 0.008	0.123 ± 0.007	0.14 ± 0.01	0.188 ± 0.008
Chromophore	P_{bot} (atm)	0.2 ± 0.1	0.21 ± 0.05	1.04 ± 0.09	1.24 ± 0.09	0.48 ± 0.05	1.24 ± 0.08
	N_{peak} (particles/g)	0.2 ± 0.1	0.018 ± 0.009	0.018 ± 0.009	0.018 ± 0.009	0.06 ± 0.02	0.03 ± 0.02
	r (μm)	0.18 ± 0.018	0.22 ± 0.2	0.21 ± 0.02	0.23 ± 0.02	0.21 ± 0.2	0.22 ± 0.02
Tropospheric cloud	P_{bot} (atm)	1.5 ± 1.25	2.36 ± 0.09	1.70 ± 0.07	1.86 ± 0.08	3.2 ± 0.1	1.89 ± 0.09
	N_{peak} (particles/g)	20.0 ± 10.0	10.5 ± 0.4	6.7 ± 0.3	6.1 ± 0.2	5.7 ± 0.3	5.6 ± 0.2
	r (μm)	1.0 ± 0.2	0.22 ± 0.01	0.22 ± 0.01	0.206 ± 0.009	0.08 ± 0.01	0.110 ± 0.007
Goodness of fit	χ^2/N_{free}		2.43	3.37	4.27	2.96	3.23

Table 8: Table of the improvement factor of retrieved parameters using model C.

Layer	Parameter	EZ	NEB	SEB	SEB transition	NEB transition
Stratospheric haze	N_{peak}	0.79	0.91	0.89	0.84	0.91
Chromophore	P_{bot}	0.52	0.83	0.86	0.77	0.87
	N_{peak}	0.03	0.03	0.03	0.32	0.07
	r	0	0	0	0	0
Tropospheric cloud	P_{bot}	0.95	0.95	0.95	0.95	0.94
	N_{peak}	0.92	0.92	0.93	0.91	0.94
	r	0.76	0.77	0.79	0.40	0.68

5. Discussion

5.1. Comparison with previous results

For model A, we obtained a less optically thick tropospheric cloud, composed of smaller particles, that is more vertically extended in the NEB transition region and less in the SEB transition region than the one retrieved by the original authors of the study. However, we obtained a similar stratospheric haze cloud with slightly larger mean particle size than what the authors obtained.

We calculated the accumulated optical depth at 900 nm as a function of pressure for each of the regions as in Anguiano-Arteaga et al. (2021) (Figure 15). For all regions, we see a decrease in the total accumulated optical depth with respect to the priors. However, the total accumulated optical depth for the stratospheric haze increases from 0.6 to 0.7 for all regions except for the SEB transition, where there is a decrease to 0.3. For the tropospheric haze, we see more variability in the optical depths from region to region. From the *a priori* value of 50 of total accumulated optical depth at the deepest layer considered in this model, we obtained 6.4 for the EZ, 3.2 for the NEB, 3.1 for the SEB, 5.3 for the SEB transition and 3.9 for the NEB transition. Our results for the accumulated optical depth of the tropospheric haze are an order of magnitude smaller than those obtained by Anguiano-Arteaga et al. (2023). While this can be in part explained by the fact that we are analysing a different region of Jupiter, the differences are substantial enough to support that the inclusion of longer wavelengths than in Anguiano-Arteaga et al. (2023) requires a less dense tropospheric particle population. We initially tested limiting the retrievals to up to 1 micron, and we found reasonable fits ($\chi^2/N_{free} \sim 1$ or less), with most of the retrieved parameters within the a priori uncertainties. For example, the most significant changes for the EZ with respect to our results are: Model A's stratospheric haze cloud base abundance increased to 1.6 ± 0.2 particles/g; the uncertainty on the cloud base pressure reduced significantly; for the tropospheric haze the fsh decreased one order of magnitude and the cloud base abundance increased one order of magnitude; the mean particle size of both hazes became of the same order of magnitude, with tropospheric haze one increasing to 0.47+-0.01 microns, being larger than the stratospheric haze mean particle size. We also saw a decrease in the imaginary refractive indexes for the stratospheric haze, but within a priori uncertainties. Similar behaviour was also observed with the other models as well, with most parameters converging to values within the a priori uncertainties or within the uncertainties of the results presented here. The obtained pressure levels for when the accumulated optical depth is equal to unity are higher than those calculated from the prior profiles, as well as those of Regions 5 and 6 in Anguiano-Arteaga et al. (2023), regions corresponding to featureless areas in the South Tropical Zone, clear of storms and cyclones. This indicates that this model is more sensitive to deeper atmospheric levels. The deepest, at 0.38 atm in the SEB transition, and the closest to the *a priori* (0.15 atm), is located in the NEB transition region at 0.17 atm. The retrieved mean particle size (r) and peak density (N_{peak}) of tropospheric clouds are an order of magnitude smaller than the authors' for all regions. While for the mean particle size (r) the improvement factor is not as significant (see Table 4), with the exception of the SEB transition region, where the uncertainties are reduced significantly, the retrieved cloud peak densities have reduced uncertainties from the prior value. Like our results for the total accumulated optical depth, these results support that the model to fit this wavelength range requires a less particle-dense tropospheric haze across all regions, which is unlikely due to analysing a different region of Jupiter than in Anguiano-Arteaga et al. (2023). However, our results for the total accumulated optical depth for the stratospheric haze are in agreement with the results from Anguiano-Arteaga et al. (2023). We also have agreement in our mean particle sizes (r) for the stratospheric haze, for they are close to the one obtained by the authors of the study, albeit slightly larger. The retrieved pressure of the cloud base layer (P_{bot}) of the stratospheric haze is also in agreement, as well as the peak density (N_{peak}).

When comparing our obtained imaginary refractive index spectra (Figure 9) with the results from Anguiano-Arteaga et al. (2023), it must be noted that the bulk of the haze attenuation occurs outside the wavelength range of the observations used in this study. We are only sensitive to the smaller effects that extend up to 0.6 μm. For the tropospheric haze, we are in agreement for all regions. However, for the stratospheric haze, our modelling requires a large increase in attenuation, especially at 0.5 μm, with the attenuation surpassing even what the authors obtained for the Great Red Spot. This occurs for the NEB, SEB and SEB transition regions. From the results of the improvement factor calculations (Figure 10), we see that these regions are more sensitive to the attenuation at 0.5 μm than the other two. More interestingly, this is also verified at 0.6 μm albeit now with even larger improvement factors for all regions. This almost correlates with the regions in our study that have a more reddish colouration, with some considerations for the SEB transition region that has observations that are in between the EZ and SEB. Unexpectedly, this is not verified in the NEB transition, whose observations were located between the NEB and the North Tropical Zone, where some blue-absorbing effects should play a more important role, similar to the SEB transition. This model, when applied to

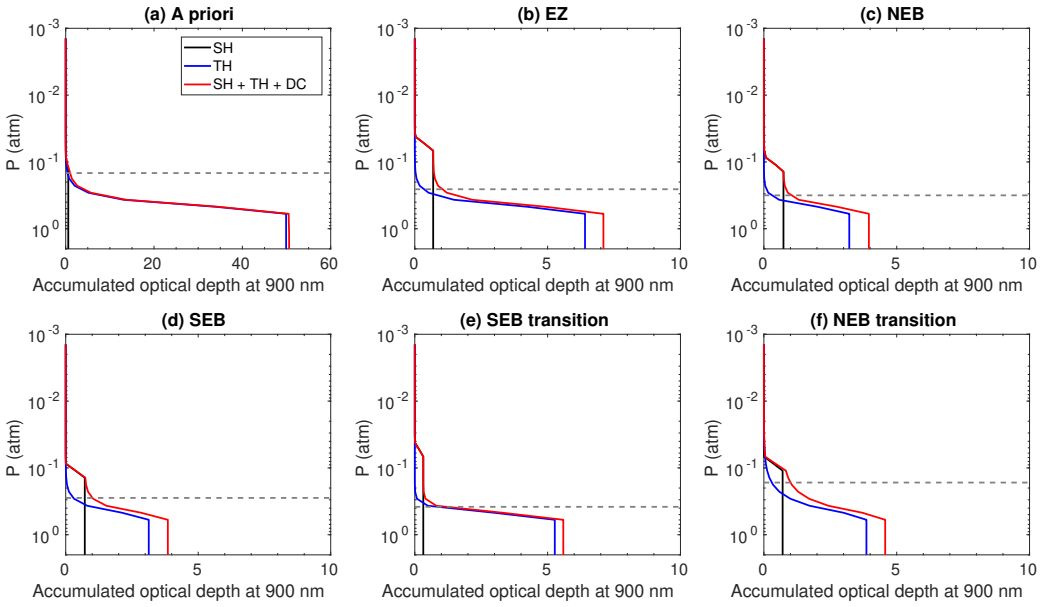

Figure 15: Comparison between the *a priori* accumulated optical depth at 900 nm as a function of pressure (atm) and the retrieved results for each region for model A. In black we have the stratospheric haze (SH) optical depth, in blue the tropospheric haze (TH) optical depth and red the total (SH + TH + DC) optical depth. The grey dashed line indicates the pressure level where the total accumulated optical depth is equal to one.

our observations, is very sensitive to the parametrisation of the stratospheric haze, with the tropospheric haze playing a minimal role in the blue attenuation observed in the spectra, as shown in Figure 10.

For model B, our results show less variability of the vertical level of the chromophore from region to region, as well as less variation in the mean particle size (r) of the deep cloud when compared with the results presented by Braude et al. (2020). The mean particle size (r) of the haze is larger across all regions, and the ammonia gas shows less abundance (nh_3v) variability than what the authors found. It must be noted that there is a correlation between the amount of NH_3 gas and the altitude of the cloud. The higher in altitude the cloud forms, the more gas it requires to sustain it. The population of aerosols, however, is independent of the NH_3 gas amount below the "knee" level. In addition, we have a more optically thick haze, with the optical depth/atm at the bottom layer of this aerosol being significant when compared to the vertical profiles in the study. This feature is the dominant parameter across all regions, in conjunction with the haze's mean particle size (r), that dominates the retrieval using this model.

We calculated the optical depth/atm at 0.89 μm as a function of pressure to compare with the profiles obtained by Braude et al. (2020). We see an overall increase in optical depth due to an increase in abundance of the aerosols at the bottom layer of the haze at 0.14 atm across all regions, with the EZ and SEB regions where this increase is the highest, when compared with the *a priori* profile. All profiles follow a similar shape, with a thick layer at 2 atm due to the deep cloud, a slightly less thick layer close to the boundary layer between the deep cloud and the haze around 0.25 atm, and a thicker layer above it near 0.1 atm due to the haze. This intermediate layer is where the chromophore layer is located and causes a slight increase in the optical depth/atm when its presence is considered. The profile retrieved from the EZ is the most optically thick overall, with an increase in thickness for the layer at 2 atm, while the one retrieved for the NEB is the thinnest. The SEB shows the most optically thick haze bottom layer, with the optical depth/atm reaching close to the values of the thick layer due to the deep cloud. Comparing now with the results from Braude et al. (2020), the authors do not see an increase in optical depth/atm at the bottom layer of the haze, having an almost constant value of 1 across all pressure levels. For the case of the NEB, our results disagree with the findings of the authors. We do not see the inversion between the deep 2 atm layer and the intermediate 0.25 atm layer. The authors' vertical profile decreases uniformly from 1 atm until the boundary between the deep cloud and haze, where it stays constant at a value lower than 1 optical depth/atm. Furthermore, our most optically thick layer is located deeper and is more

opaque than the level where the optical depth per atm obtained by the authors is largest. Adding to this, the location of the chromophore layer obtained by the authors is found deeper in the atmosphere at around 0.6 atm, extending from 0.2 atm to 0.8 atm, while ours remains at the *a priori* level of 0.25, as per our improvement factor results (Table 6), the model is not very sensitive to the parametrization of the chromophore for this wavelength range. However, our results for the EZ are mostly in agreement with those found by the authors, except for the haze. The chromophore layer is located at the same pressure level, and the optical depth/atm values for the 2 atm layer and 0.25 atm layer are in agreement.

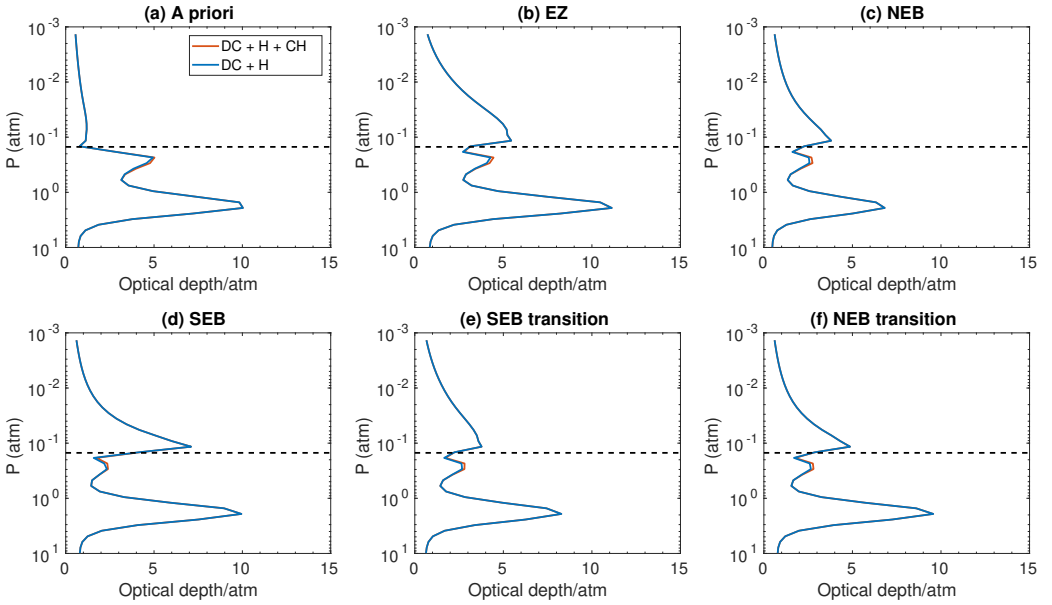

Figure 16: Comparison between the *a priori* aerosol vertical profiles and the retrieved profiles for every region for model B. We compare the optical depth/atm at 0.89 μm with the presence of the chromophore (DC + H + CH) and without (DC + H). The horizontal dashed line corresponds to 0.15 atm, separating the deep cloud layer from the haze.

Comparing now the results shown in Table 5 with the ones obtained by Braude et al. (2020), we obtained a larger mean particle size (r), as in model A, across all regions for the haze, than those by the authors' limb-darkening analysis. Our retrieved chromophore mean particle sizes (r) are smaller than those obtained by the authors. Our retrieved peak pressure level for the chromophore ($P(\rho_{max})$) for the NEB is in disagreement. The authors obtained a pressure level deeper, at 0.60 atm, compared to our retrieved value of 0.24 atm. The deep cloud mean particle size (r) differs from the 1.5 μm that the authors obtained, compared to our retrieved size of 4.40 μm for the NEB region. Comparing the VMR of the ammonia gas profile from Braude et al. (2020) with our results proves to be difficult. The authors show the VMR at 1 bar and how it varies with latitude. Our observation scheme is not as sensitive to latitudinal variations across different belts/zones. Nonetheless, we can still say if our values are within the interval of values for each common region in our and the authors' studies. For all regions other than the EZ and NEB, all our retrieved VMRs of ammonia gas at 1 bar are below the minimum value obtained by the authors, approximately 4.0×10^{-5}.

Lastly, for model C, we retrieved a similarly dense stratospheric haze, except for the SEB and SEB transition regions, a deeper, less dense chromophore layer, composed of larger particles, and a deeper, also less dense, deep cloud composed of particles of the same size or, in some regions, even smaller particles than those of the chromophore layer.

Our results show a deeper chromophore layer (P_{bot}) than what Pérez-Hoyos et al. (2020) found at 0.14 atm across all latitudes in their study. Our highest retrieved pressure level is located at the EZ at 0.21 atm, and the deepest ones, reaching over 1 atm, are located at the NEB, SEB and NEB transition regions. Our retrieved mean particle size (r) of the chromophore is more than double across all regions compared to the authors' 0.1 μm mean particle size (r). Our deep cloud is found to be deeper(P_{bot}) than what was presented by the authors. They found the deep cloud to be located

around 1 atm, whilst the highest deep cloud we retrieved was located at 1.7 atm for the NEB and the deepest at 3.2 atm at the SEB transition. The authors also found little variation in the mean particle size (r) of the deep cloud (1.35 μm), unlike our results, where we obtain mean particle sizes (r) an order of magnitude smaller, with the smallest being found at the SEB transition with a mean particle size (r) of 0.08 μm. The high sensitivity to the parameters of the deep cloud and convergence towards unphysical results of the mean particle size and cloud base abundance (N_{peak}) likely stems from limitations of the "Crème Brûlée" atmospheric model itself when applied to this spectral region.

We compared the aerosol profiles, both *a priori* and retrieved, of model A and model B across all regions considered. Unfortunately, model C's configuration does not require nor produce aerosol profiles, so it can't be considered in this comparison. Figure 17 shows the *a priori* and the retrieved aerosol profiles for each region for model A and model B. The model B profiles present in the figure in blue are similar to the ones in Figure 16, considering the three aerosol populations, albeit now for 0.9 μm. Model A's profiles consider only the contribution from the stratospheric haze and tropospheric haze. We see that model A's *a priori* profiles are orders of magnitude more optically thick than the ones from model B, with very thick tropospheric haze near 0.5 atm when compared to model B's deep cloud. However, we see similar behaviour between both models when performing retrievals. We see an increase in the optical depth of the top-most aerosol population while the deepest aerosol species converge towards similar optical depth per pressure values, albeit at different pressure levels. Model A's stratospheric haze almost doubled its optical depth, surpassing the optical depth values found in the retrievals with model B, when comparing to the almost 5 times increase from the bottom layer of model B's haze.

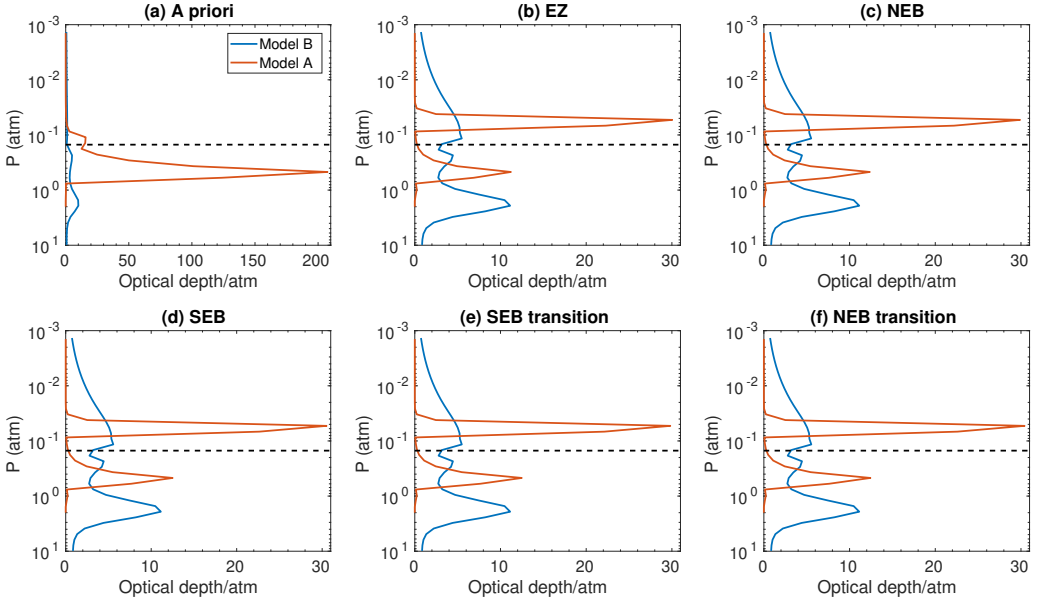

Figure 17: Comparison between the *a priori* aerosol vertical profiles and the retrieved profiles for every region for models A and B. We compare the optical depth/atm at 0.90 μm of model B with all three aerosol populations considered and model A's stratospheric and tropospheric hazes. The horizontal dashed line corresponds to 0.15 atm, separating model B's deep cloud layer from the haze.

From these comparisons, a few common aspects can be concluded. All three models are very sensitive to the highest haze properties and parametrisation. The models seem to require the presence of aerosols constituted by larger particles above aerosols made from smaller particles. The models also are not as equally sensitive to the intermediate aerosol, with model A being more sensitive to cloud base abundance (N_{peak}) and model C to the cloud base pressure level (P_{bot}), while model B is not sensitive at all. We must note that across all models, the current parametrisation is not sufficient to fully explain the observations. Across all models and regions, no fit achieved a χ^2/N_{free} close to unity. For this reason, our results should not be fully conclusive, but at least provide some indication of what aerosols are responsible for the features observed in the spectra. It must also be noted that the discrepancies between our results

and those of the original authors of the models are likely due to differences in spectral coverage and, to a lesser degree, differences in the regions covered in our study relative to the original works.

There are other works that locate the haze layers higher in the Jovian atmosphere. Zhang et al. (2015) located aerosol heating peaks at around $\sim$ 10 hPa (approximately 0.01 atm), in a stratospheric haze layer. Our results, and *a priori* values for the models whose haze's cloud base pressure is fixed, are an order of magnitude larger. The retrieved cloud base pressures (P_{bot}) for the stratospheric haze of model A are the closest to the results found by Zhang et al. (2015), with the cloud base pressure converging towards 0.06 atm for the EZ and SEB transition regions, albeit with large uncertainties. Other regions converge towards 0.1 atm. Model B's haze cloud base pressure is fixed around 0.15 atm when the deep cloud profile transitions to the haze profile. And model C's fixes the cloud base of the haze of the Crème Brûlée model at 0.2 atm. However, the work by Zhang et al. (2015) includes high-phase angles and UV wavelengths, which are sensitive to higher levels, due to Rayleigh scattering, and smaller particles. Phenomena which we are not sensitive to, due to the wavelength range considered in our study.

5.2. Inter-model comparison

Overall, the best model of the three to fit the observations, quantitatively, is model B, for it has the lowest χ^2/N_{free} values across all regions, despite being the model with the most free parameters.

The parametrisation of the aerosol at the highest altitude of each model plays a significant role in fitting the synthetic spectra to the observations, as shown in the improvement factor tables (Tables 4, 6 and 8).

Model B suggest the presence of a more optically thick haze composed of larger particles, while model C's results show that such a haze is not required. There is an indication that the deeper in the atmosphere the aerosol layer is located, the larger the particles will be, when comparing the mean particle size (r) of model B with the mean particle size (r) of model C, whose stratospheric haze is approximately located at 60 km, which is expected.

Models A and C are significantly sensitive to the parametrisation of the chromophore layers, as shown in Tables 4 and 8. Model A is sensitive to the cloud base abundance (N_{peak}) of the tropospheric haze chromophore and the cloud base abundance (N_{peak}) and mean particle size (r) of the stratospheric haze chromophore, while model C is more sensitive to the cloud base pressure (P_{bot}). Model A indicates the presence of a more opaque upper-layer chromophore and a less opaque lower-layer chromophore, albeit more opaque than model C, while model C's chromophore layer altitude varies from region to region, with the highest at the whitest regions (EZ and SEB transition) and the deepest at the reddest (NEB, SEB and NEB transition). The models show distinct results from one another, especially given the distinct way the chromophore is parametrised by each of the models. Model B shows a lack of sensitivity towards the chromophore parameters, likely due to the small particle size of this aerosol population when compared to the other models, coupled with the spectral coverage of this study.

Lastly, regarding the deeper aerosol layer, we find that only model C is significantly sensitive to the properties of the tropospheric cloud. The retrieved mean particle sizes (r) are similar to those of the chromophore of the same model. The retrieved cloud base opacities (N_{peak}) show a decrease from the *a priori* value while the cloud base pressure (P_{bot}) shows an increase. The mean particle size is unusually small for what is expected for the tropospheric cloud layer. We have a similar occurrence with model A's stratospheric haze mean particle size (r) being larger than the tropospheric haze's, and with model B's haze mean particle size (r) being larger than the chromophore's. The cloud base opacities differ across all chromophore species of all models.

Table 9 compares our retrieved results for each of the models for the EZ. Model A's tropospheric haze cloud base is located at a similar pressure level as model B's and model C's chromophore cloud base. Models A (tropospheric haze) and B share the same order of magnitude for the mean particle size, while model C's is one order of magnitude larger, more in line with model A's mean particle size of the stratospheric haze. The retrieved cloud base opacities differ across all chromophore species and models. The retrieved mean particle size of the cloud of model B is one order of magnitude larger than the one retrieved with model C.

Table 9: Table comparing all retrieved parameters across the three models for the EZ, keeping similar aerosols at the same level.

Model A				**Model B**			**Model C**		
Haze				Haze	r (μm)	0.79 ± 0.02	Stratospheric haze	N_{peak} (particles/g)	0.17 ± 0.02
					σ	0.043 ± 0.004			
	Stratospheric haze	P_{bot} (atm)	$0.06^{+4.14}_{-0.06}$		ρ_{max} ($\times 10^{-4}$) (particles/g)	5.2 ± 0.6	Chromophore	N_{peak} (particles/g)	0.018 ± 0.009
		N_{peak} (particles/g)	0.66 ± 0.05						
		fsh	0.09 ± 0.1						
Chromophore				Chromophore	$P(\rho_{max})$ (atm)	0.23 ± 0.03		P_{bot} (atm)	0.21 ± 0.05

		r (μm)	0.409 ± 0.008						
	Tropospheric haze	P_{bot} (atm)	$0.5^{+0.3}_{-0.2}$		r (μm)	0.044 ± 0.004		r (μm)	0.22 ± 0.2
		N_{peak} (particles/g)	2.8 ± 0.1						
		fsh	0.24 ± 0.04		σ	0.1 ± 0.01			
		r (μm)	0.086 ± 0.009						
Cloud	Tropospheric cloud	S ($\times 10^{-3}$)	0.77 ± 7.71	Deep cloud	r (μm)	4.45 ± 0.05	Tropospheric cloud	P_{bot} (atm)	2.36 ± 0.09
								N_{peak} (particles/g)	10.5 ± 0.4
								r (μm)	0.22 ± 0.01

Model B achieved the best fit across all regions, being the model with the most free parameters (35). Model C had the worst fits with the fewest free parameters (7) of the models addressed here. This can be an indication of overfitting for the case of model B. However, it must be noted that N_{free} is still big enough when compared to the number of free parameters of each of the three models, so overfitting should not be a major concern.

All three models show a high sensitivity to the highest altitude aerosol, regardless of atmospheric or aerosol configuration. This is an interesting result, indicating a dominance of spectral features due to aerosols located at the tropopause or above. We also obtained particle sizes that appear unphysical, with hazes composed of larger particles located above hazes and clouds with smaller particles. This could be an indication of the limitations of the models when applied to this specific spectral range or that we are blind to the spectral features coming from deeper in the atmosphere.

5.3. Sensitivity analysis

The first point that we wanted to address here is that not all models used in this work have the same atmospheric scheme and number of gases. We tested the atmosphere configuration of model B on model A for the EZ to see if any major differences were observed in the retrieved results or fit of the spectra. In Figure 18, we show the resulting fit for the EZ. This resulted in a slightly worse fit, with a χ^2/N_{free} of 2.20 compared to the original 2.04. Some parameters were changed beyond the error bars of the original configuration. For the stratospheric haze retrieval, there is an increase in attenuation at 0.6 μm observed in the retrieved imaginary refractive index spectrum from $(0.5 \pm 0.1) \times 10^{-2}$ to $(0.7 \pm 0.1) \times 10^{-2}$. For the tropospheric haze, we see an increase of the peak density from 2.8 ± 0.1 particles/g to 7.3 ± 0.3 particles/g, the fsh decreased from 0.24 ± 0.04 to 0.13 ± 0.03, and the mean particle size (r) increased from 0.086 ± 0.009 μm to 0.24 ± 0.02 μm. With this, we have a more absorbing stratospheric haze and a less vertically extended and more dense tropospheric haze composed of larger particles. However, with the worsening of the fit, we can conclude that the atmospheric scheme is not the main factor responsible for the fits not having a χ^2/N_{free} close to unity. Model B was the model that achieved the best fits overall. However, applying the atmospheric gaseous configuration to model A, we see a slight worsening of the fit, even though model B is a more complete description of the Jovian atmosphere, indicating that the main contributor to the fits is the aerosol scheme rather than the composition of the atmosphere. Including other chemical species in the atmospheric scheme will likely not lead to a significant improvement of the models for this wavelength range.

We also performed a bracketing analysis of the most sensitive parameters of each of the models for the EZ, the best fitting region (improvement factor > 0.60) and for the SEB, the worst fitting region. This analysis consists of changing the prior value by a certain amount, plus 10 % and minus 10 % in this case, to test if the prior is a good estimate and still converges to the retrieved results.

For model A, we performed the analysis on the stratospheric haze's cloud base abundance (N_{peak}) and mean particle size (r), and the tropospheric haze's cloud base abundance (N_{peak}). For the EZ region, the retrieved stratospheric haze cloud base abundance (N_{peak}) values that are in agreement show a cloud base abundance (N_{peak}) of 0.66±0.05 particles/g, as shown in Table 3, 0.68±0.08 particles/g for the +10 % configuration and 0.65±0.05 particles/g for the -10 %. For the stratospheric haze mean particle size (r), we see a slight loss in precision when performing the bracketing and a decrease in the retrieved values for both cases. The obtained values are not in agreement but are very close to each other, when comparing the 0.409±0.008 μm from the results with the 0.37±0.01 μm from the +10 % retrieval and with the 0.39±0.01 μm from the -10 %. Lastly, for the tropospheric haze cloud base abundance (N_{peak}), all retrieved values are in agreement, with 2.8±0.1 particles/g for the results, 2.9±0.1 particles/g for the +10 % retrieval and 2.7±0.1 particles/g for the -10 % one. For all the priors analysed, the synthetic spectra match the nadir geometry. However, some minor differences are observed for the limb viewing geometry. These differences are smaller than the *a priori* uncertainties of the observation spectra and the confidence in the retrievals is preserved. The obtained χ^2/N_{free} values for this bracketing analysis is shown in Table 10. For the SEB region, for the stratospheric haze cloud base abundance (N_{peak}), the value of the +10 % (0.80±0.06 particles/g) bracketing is in agreement, although larger, with the results

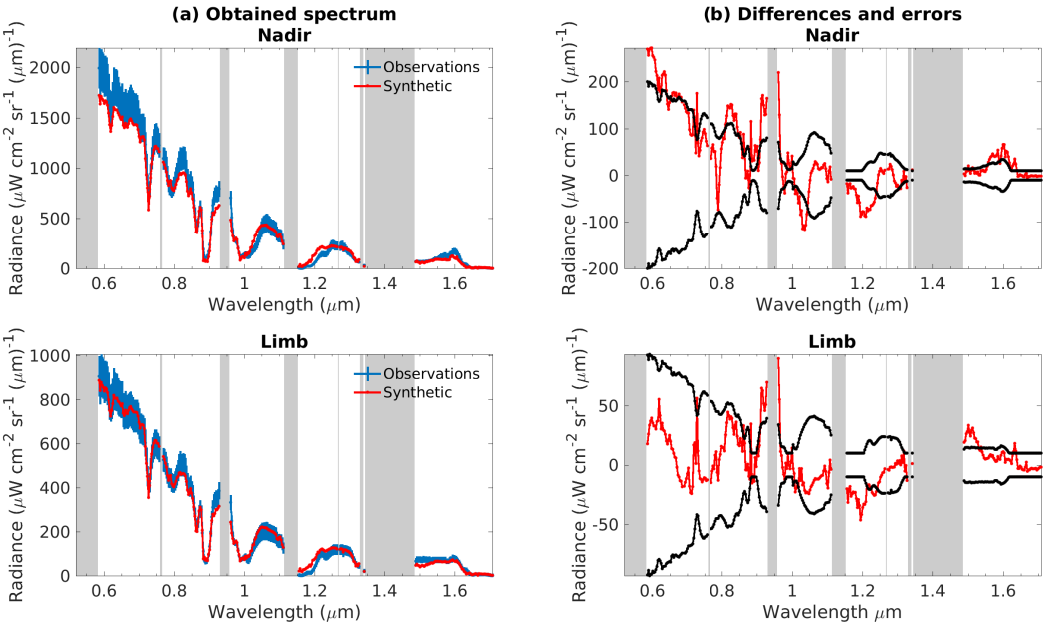

Figure 18: Comparison between observed (blue) and modelled (red) spectra (left column) and comparison between differences (red) and *a priori* errors (black) (right column) for the EZ using model A with the layering and compositional scheme from model B, with the grey shaded areas corresponding to telluric absorption. The top row corresponds to nadir (incidence and emission angle = 0°) and the bottom row to limb (incidence and emission angle = 61.45°).

(0.70± 0.09 particles/g). However, for the -10 % bracketing the cloud base abundance converged to an even larger value (1.03±0.06 particles/g) with a worsening of the goodness of fit (χ^2/N_{free}), as seen in Table 10. Despite the agreement with the results of the cloud base abundance +10 % bracketing, there was a significant improvement of the goodness of fit with a caveat. We see a massive increase in the imaginary refractive index spectrum of the stratospheric haze from 0.9 μm to 1.7 μm with the peak at 1.5 μm, with a value of 0.9. These values far exceed the maximum value of the *a priori* imaginary refractive index spectrum at 0.6 μm, and the model is converging towards a greatly red-attenuating stratospheric haze solution that is not observed in our results and is not expected. For the stratospheric haze mean particle size (r), the -10 % bracketing (0.346±0.008 μm) is in agreement with the results (0.36±0.01), while the +10 % bracketing produced slightly smaller results 0.32±0.02. The +10 % bracketing converged to a worse solution, likely due to not converging towards an increase in the attenuation at 0.5 μm in the imaginary refractive index, like in our results. Lastly, for the tropospheric haze cloud base abundance (N_{peak}), the values do not agree. Our results of 1.35±0.06 particles/g are slightly smaller than the +10 % bracketing of 1.53±0.09 particles/g, and for the -10 % bracketing, the cloud base abundance is significantly larger than the other values (6.0±0.5 particles/g). While our results are close to those of the +10 % bracketing with similar goodness of fit, a similar effect to the stratospheric haze cloud base abundance +10 % bracketing occurs for the retrieval of the -10 % bracketing of the tropospheric haze cloud base abundance. We also see an increase in attenuation of the stratospheric haze imaginary refractive index spectrum, this time centred at 1.4 μm with a value of approximately 0.35. Overall, this analysis demonstrates that the retrievals are robust, as the parameters are not significantly driven by the initial *a priori* values. But when subjected to the worst region (SEB), some of the parameters have trouble converging due to some of the bracketing retrievals going for a solution that requires massive increases in attenuation in the stratospheric haze imaginary refractive spectrum.

For model B, the most sensitive parameter was the haze mean particle size (r). We also performed a bracketing analysis of the aerosol abundance profiles to see if the priors are adequate for the best-fitting region, EZ, and the worst, SEB. For the EZ, comparing our haze mean particle size (r) result of 0.78±0.02 μm with the result of 0.78±0.02 from the +10 % retrieval and 0.78±0.02 from the -10 % retrieval, we can say that the prior is a robust initial estimate. For the aerosol vertical abundance profile analysis, we simultaneously changed the particle abundance of both the haze and deep cloud profiles by ±10 %. The resulting vertical profiles are shown in Figure 31. We see that both bracketing

profiles match very closely with the one from our results, with some small deviations observed at 0.25 atm and 2 atm, where the deep cloud has an increase in optical thickness. For the SEB, the mean particle size (r) of the haze retrieved for the bracketing analysis is in agreement with our result, 0.64±0.02 μm for the +10 % bracketing, 0.66±0.02 μm for the -10 % bracketing, and 0.65±0.02 μm for our result. Regarding the vertical abundance, the results are shown in Figure 31. We see that the profiles start to slightly deviate from each other above the 2 atm level, but retain their overall shape. Like in model A, the robustness of the retrievals is confirmed, for the bracketing results deviate little from our results for the EZ and SEB, while keeping a consistent goodness of fit as shown in Table 10.

For model C, the most sensitive parameters being considered for this bracketing analysis are the stratospheric haze cloud base abundance (N_{peak}), the tropospheric cloud base pressure (P_{bot}) and base abundance (N_{peak}). For the EZ, the stratospheric haze cloud base density result, 0.17±0.02 particles/g, is in agreement with the +10 % retrieval, 0.19±0.01 particles/g, and the -10 % retrieval result, 0.17±0.02 particles/g, as well. The cloud base pressure (P_{bot}) for the tropospheric cloud is in agreement as well with our results of 2.36±0.09 atm, 2.3±0.1 atm for the +10 % and 2.45±0.08 atm for the -10 % retrieval. Lastly, we also have agreement in the retrieved tropospheric cloud base abundance (N_{peak}), 10.5±0.4 particles/g for our results, 10.4±0.4 particles/g for the +10 % retrieval and 10.6±0.4 particles/g for the -10 %. The resulting χ^2/N_{free} are shown in Table 10. For the case of the SEB, the stratospheric haze cloud base abundance (N_{peak}) result, 0.123±0.007 particles/g, is in agreement with the +10 % bracketing, 0.124±0.007 particles/g, and the -10% bracketing, 0.130±0.007 particles/g. The cloud base pressure (P_{bot}) for the tropospheric cloud is in agreement as well with our results of 1.86±0.08 atm, for the -10 % retrieval, 1.84±0.08 atm, but not with the +10 ± bracketing, where the retrieved base pressure was higher (2.23±0.09 atm). The retrieved tropospheric cloud base abundance (N_{peak}), 6.1±0.2 particles/g for our results, is in agreement with the retrieval from the -10 % bracketing (6.4±0.2 particles/g); however, the +10 % bracketing retrieved a higher value for the cloud base abundance (6.7±0.3 particles/g). The resulting χ^2/N_{free} are shown in Table 10. This confirms, similarly to models A and B, that the retrievals are robust and they do not depend significantly on the initial choice of *a priori* values with some minor discrepancies.

6. Conclusions

We performed, for the first time, flux calibration of Solar System CARMENES data, using Saturn's B ring as the flux calibrator. We exploited the high number of observations to perform a Minnaert limb-darkening approximation and construct synthetic Jupiter spectra at 0° and 61.45° zenith angles for five distinct regions in the atmosphere of Jupiter. This achievement shows that this instrument is apt to perform further observations of Solar System targets, with a high spectral resolution, opening the doors to future high-quality measurements.

We applied three competing atmosphere models to the Jupiter CARMENES data and found some common points between them that can give an indication of the aerosol structure present in the atmosphere of Jupiter. The main conclusions from this modelling are the following:

- The aerosol layer at the highest altitude seems to have the most influence on how the models adjust to the observation spectra across all models, especially the mean particle size as per the results from models A and B and the cloud base abundance as per models A and C. The altitude level of this aerosol layer also plays a major role in the retrieval results.

- The parametrisation of the chromophore layer also plays an important role for models A and C, but with different weights of the importance of the parameters depending on the model. Model A is more sensitive to the cloud base abundance and mean particle size, while model C is more sensitive to the pressure level at which the cloud base layer is located. However, only model A shows that the imaginary refractive index spectrum for the upper layers is significant in fitting the observations.

- The deeper aerosol layer only plays a major role in the retrievals for model C. This model is sensitive to the pressure level and abundance of the cloud base as well as the mean particle size. When compared to model B, the resulting mean particle size for the tropospheric cloud retrieved by using model C is an order of magnitude smaller.

- On average, model B appears to be the best-fitting model, with the lowest χ^2/N_{free} of 1.81 for the EZ and the highest of 3.26 for the SEB. However, none of the models achieved a χ^2/N_{free} less than 1, indicating that none of the models in this study fully represent what the observations show, most likely due to the spectral range of the CARMENES observations and longer wavelength data could change the inferred aerosol structure.

- Model C is the worst model to fit our observations, overestimating the blue absorption in all regions, despite the chromophore layer being the most sensitive to variations from region to region of all three models considered in this study.

- Model B for this spectral region might be subjected to overfitting, for only 14 of the 35 free parameters are significantly sensitive to the fits. While model C might suffer from underfitting, despite only 5 of the 7 free parameters being significantly sensitive to the fits, these few might not be enough to capture all the key spectral variations.

- Model A's retrieved cloud base pressure for the tropospheric haze is within the levels measured for the NH_3 cloud by the Galileo probe (Sromovsky and Fry, 2002). Galileo observations coupled with Hubble Space Telescope observation results show the presence of a high tropospheric haze at 120 mbar (Sromovsky and Fry, 2002), deeper than the base pressure level we obtained for the stratospheric haze of model A. The retrieved mean particle size for the stratospheric haze appears to converge towards a $\sim 0.5\ \mu m$ that is derived for the haze in Sromovsky and Fry (2002), while our retrieved particle size for the tropospheric haze is one order of magnitude smaller and goes against what is expected.

- For model B, the retrieved particle size for the deep cloud shows little variation from region to region, unlike what is seen in Braude et al. (2020), where for the darker regions the mean particle size ranges between 1–2 μm while for the lighter regions the particle size ranges between 3–4 μm. However, Sromovsky and Fry (2002) shows that the upper cloud, corresponding to the putative ammonia-ice cloud, should have an effective radius of 0.25–0.5 μm, and that the particle sizes both retrieved here and in Braude et al. (2020) are of the same scale of the effective radius of the particles that make up the middle cloud, putative of NH_4SH. Our retrieved chromophore pressure level of the peak specific density close to the one retrieved by Braude et al. (2020) for the GRS and not

as deep as they found for regions outside of it. Our retrieved haze mean particle size is found to be larger than the ones retrieved by Braude et al. (2020), while results by Zhang et al. (2015) show that, from 40°S to 25°N, there is an optically thin aerosol layer concentrated around 0.05 atm composed of compacted particles with radii ranging in 0.2–0.5 μm

- The retrieved model C's tropospheric cloud base pressure is located at a similar pressure as the NH_4SH cloud level from Atreya et al. (1998) and deeper than the cloud detected from the Cassini Composite Infrared Spectrometer (CIRS) experiment (Matcheva et al., 2005), but within the expected limits of the cloud layer of the best fitting models from Baines et al. (2019). With the particle size being slightly smaller than the effective radius for the upper cloud (putative ammonia-ice) from Sromovsky and Fry (2002). The retrieved chromophore base pressure is in agreement with the one from Baines et al. (2019), but the retrieved mean particle size was slightly larger.

- We retrieved unusually smaller tropospheric cloud particles for model C and unusually larger stratospheric haze particles for models A and B. These results can be potentially unphysical, likely due to the limitations of the models when applied to this wavelength range.

Taking all these conclusions into account, we find that we require models that better describe the Jovian atmosphere that consider spectra from UV, constraining the chromophore opacity, vertical distribution and particle size, to thermally emitted IR, constraining the deeper clouds that have larger particles, holistically, complementing the blue-absorption features found at shorter wavelengths with the overall scattering occurring at longer wavelengths, and taking into account limb-darkening behaviour. The models used in this work are limited in the shape of the aerosol particles considered and future work should explore different particle morphologies and higher phase angles to see which better capture aerosol radiative effects. This kind of investigation probably requires a careful analysis of the assumptions usually taken on the number and nature of aerosol layers, as well as the parameters defining their properties. Such an analysis would be a complex task that would require combining very different observations and new modelling approaches, like a Bayesian inference of the *a posteriori* space to arrive to a satisfactory solution, but it is within the current capabilities and should be pursued in the near future to avoid the multiplicity of solutions for the spatial distribution of aerosols in the Jovian atmosphere.

7. Acknowledgments

This work was supported by Fundação para a Ciência e Tecnologia (FCT) of reference PTDC/FIS-AST/29942/2017, through national funds and by FEDER through COMPETE 2020 of reference POCI-01-0145-FEDER-007672, and through the research grants UIDB/04434/2020, UIDP/04434/2020 and UID/04434/2025, José Ribeiro acknowledges support from the Fundação para a Ciência e Tecnologia (FCT) through the Fellowship 2021.04584.BD, Santiago Peréz-Hoyos acknowledges funding by the grant PID2023-149055NB-C31, funded by MICIU/AEI/10.13039/501100011033 and FEDER, UE and by Elkartek grant KK-2025/00106, from the Basque Government, Asier Anguiano-Arteaga acknowledges support by the Programa de Perfeccionamiento de Personal Investigador Doctor del Gobierno Vasco, Patrick Irwin acknowledges the United Kingdom Science and Technology Facilities Council (STFC) for funding (ST/S000461/1). We acknowledge the opportunity to use and process the observations made with CARMENES instrument at the Calar Alto Observatory.

A. Plots of fits to other regions

A.1. Model A

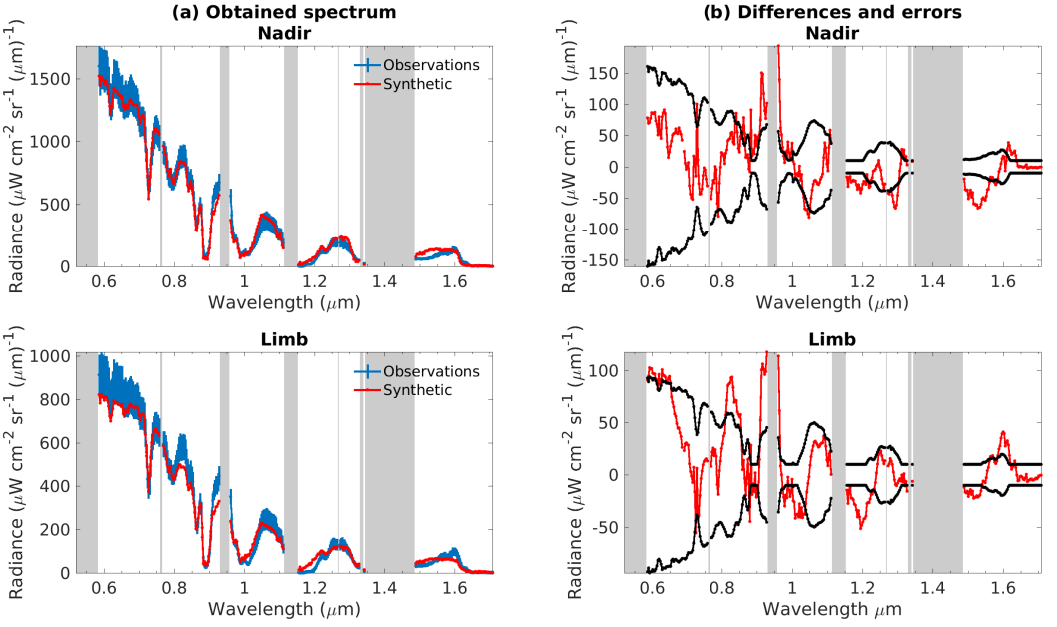

Figure 19: Comparison between observed (blue) and modelled (red) spectra (left column) and comparison between differences (red) and *a priori* errors (black) (right column) for the NEB using model A, with the grey shaded areas corresponding to telluric absorption. The top row corresponds to nadir (incidence and emission angle = 0°) and the bottom row to limb (incidence and emission angle = 61.45°).

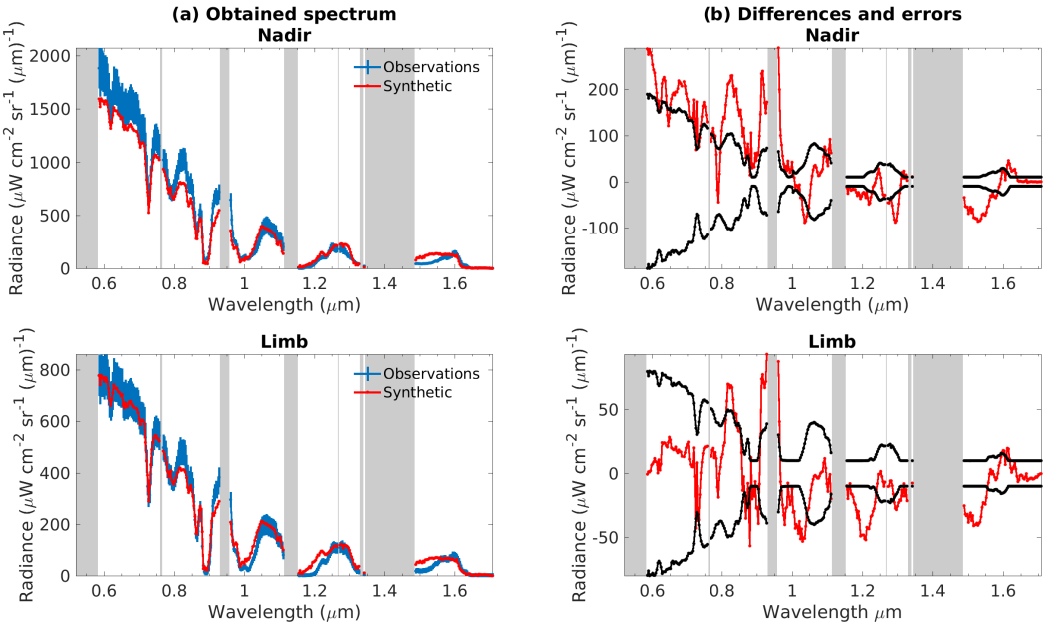

Figure 20: Comparison between observed (blue) and modelled (red) spectra (left column) and comparison between differences (red) and *a priori* errors (black) (right column) for the SEB using model A, with the grey shaded areas corresponding to telluric absorption. The top row corresponds to nadir (incidence and emission angle = 0°) and the bottom row to limb (incidence and emission angle = 61.45°).

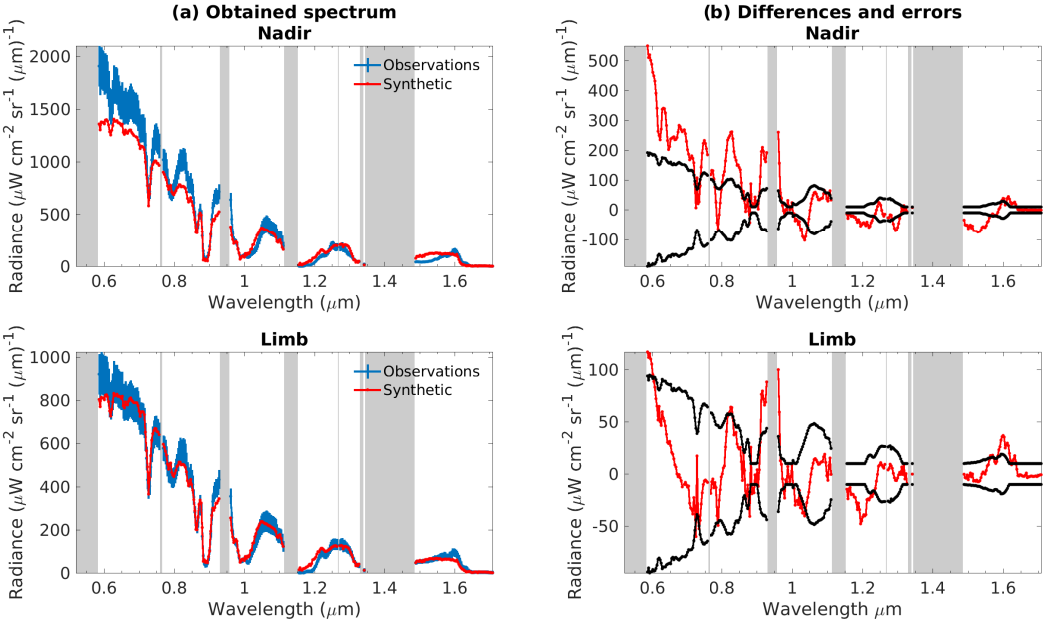

Figure 21: Comparison between observed (blue) and modelled (red) spectra (left column) and comparison between differences (red) and *a priori* errors (black) (right column) for the SEB transition using model A, with the grey shaded areas corresponding to telluric absorption. The top row corresponds to nadir (incidence and emission angle = 0°) and the bottom row to limb (incidence and emission angle = 61.45°).

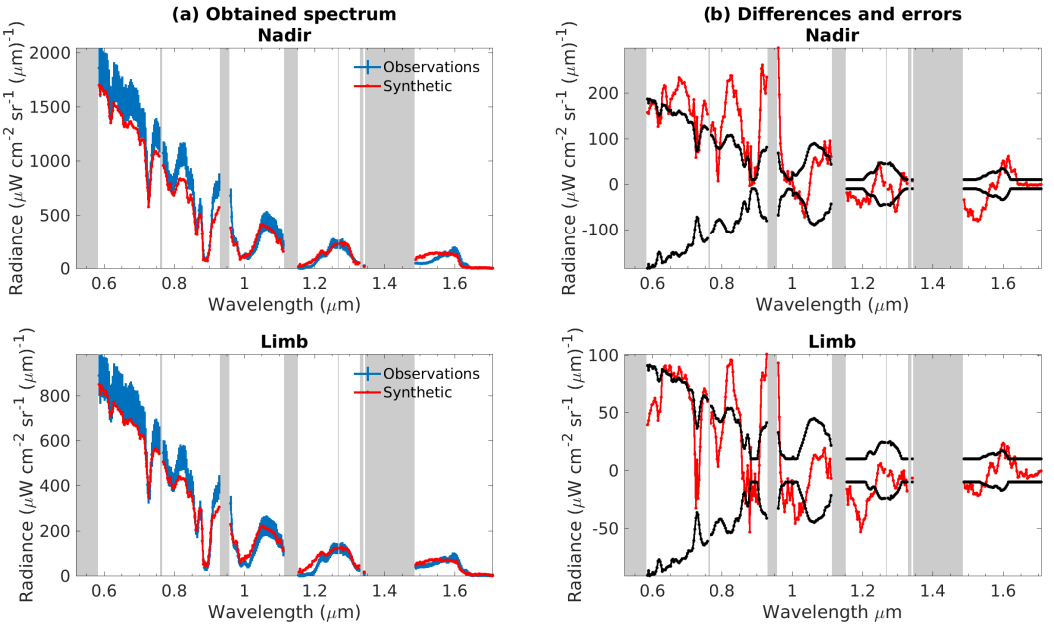

Figure 22: Comparison between observed (blue) and modelled (red) spectra (left column) and comparison between differences (red) and *a priori* errors (black) (right column) for the NEB transition using model A, with the grey shaded areas corresponding to telluric absorption. The top row corresponds to nadir (incidence and emission angle = 0°) and the bottom row to limb (incidence and emission angle = 61.45°).

A.2. Model B

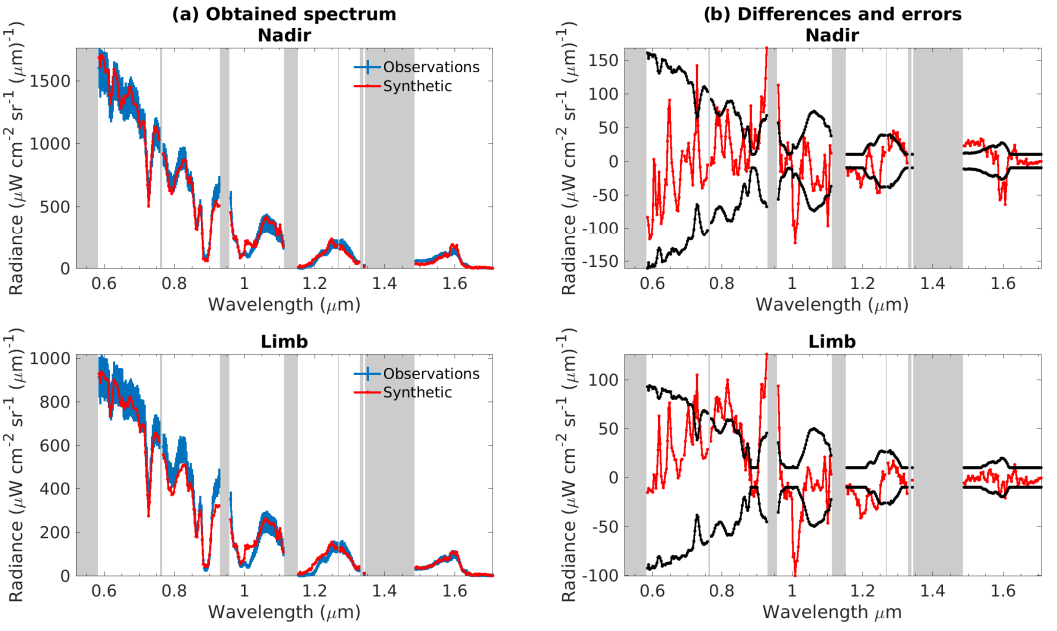

Figure 23: Comparison between observed (blue) and modelled (red) spectra (left column) and comparison between differences (red) and *a priori* errors (black) (right column) for the NEB using model B, with the grey shaded areas corresponding to telluric absorption. The top row corresponds to nadir (incidence and emission angle = 0°) and the bottom row to limb (incidence and emission angle = 61.45°).

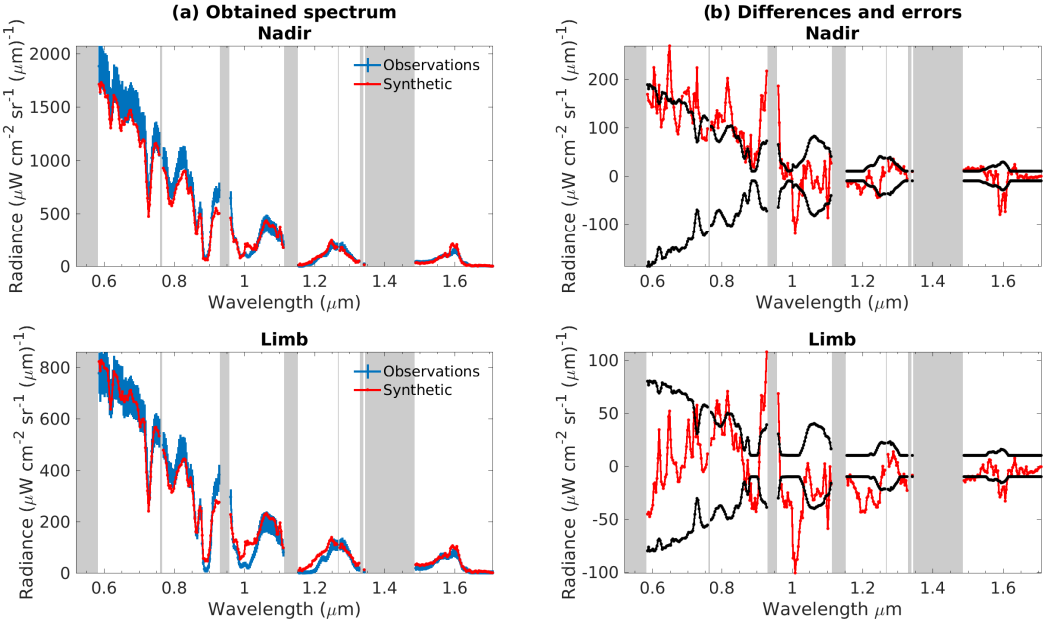

Figure 24: Comparison between observed (blue) and modelled (red) spectra (left column) and comparison between differences (red) and *a priori* errors (black) (right column) for the SEB using model B, with the grey shaded areas corresponding to telluric absorption. The top row corresponds to nadir (incidence and emission angle = 0°) and the bottom row to limb (incidence and emission angle = 61.45°).

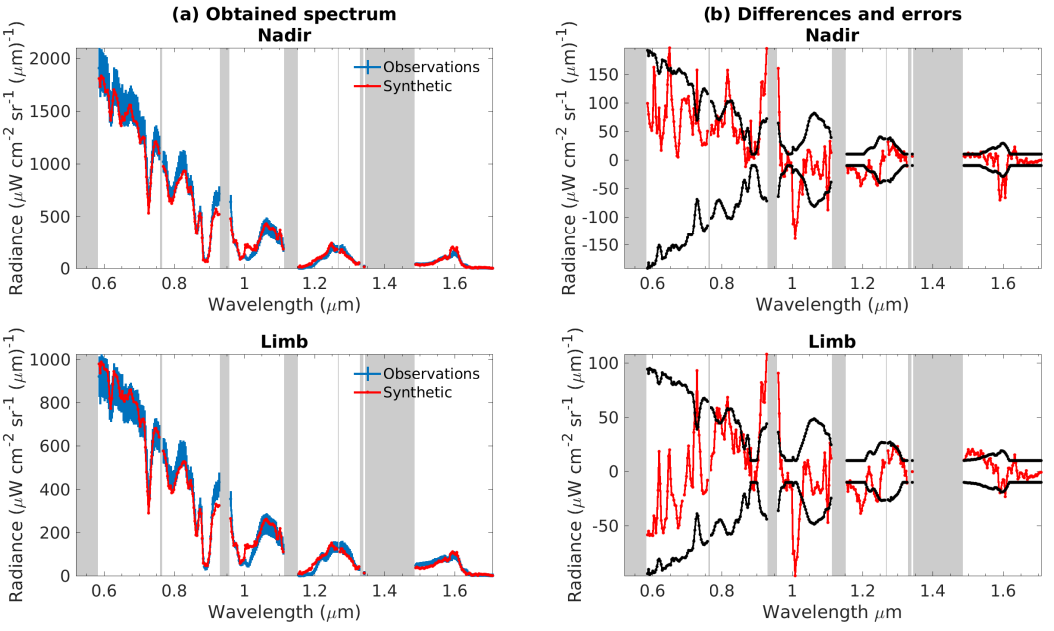

Figure 25: Comparison between observed (blue) and modelled (red) spectra (left column) and comparison between differences (red) and *a priori* errors (black) (right column) for the SEB transition using model B, with the grey shaded areas corresponding to telluric absorption. The top row corresponds to nadir (incidence and emission angle = 0°) and the bottom row to limb (incidence and emission angle = 61.45°).

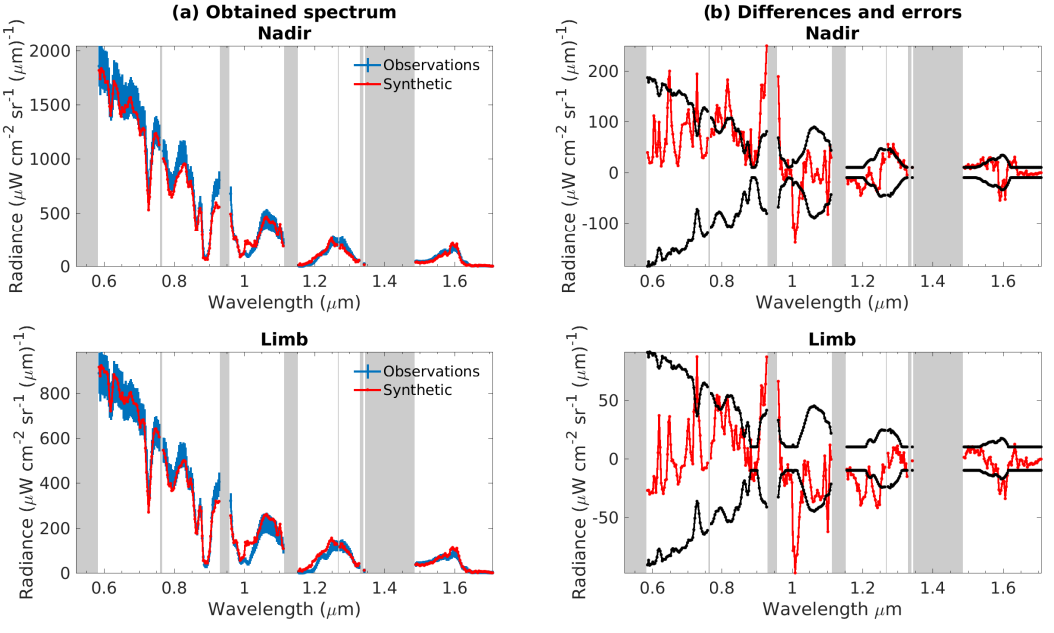

Figure 26: Comparison between observed (blue) and modelled (red) spectra (left column) and comparison between differences (red) and *a priori* errors (black) (right column) for the NEB transition using model B, with the grey shaded areas corresponding to telluric absorption. The top row corresponds to nadir (incidence and emission angle = 0°) and the bottom row to limb (incidence and emission angle = 61.45°).

A.3. Model C

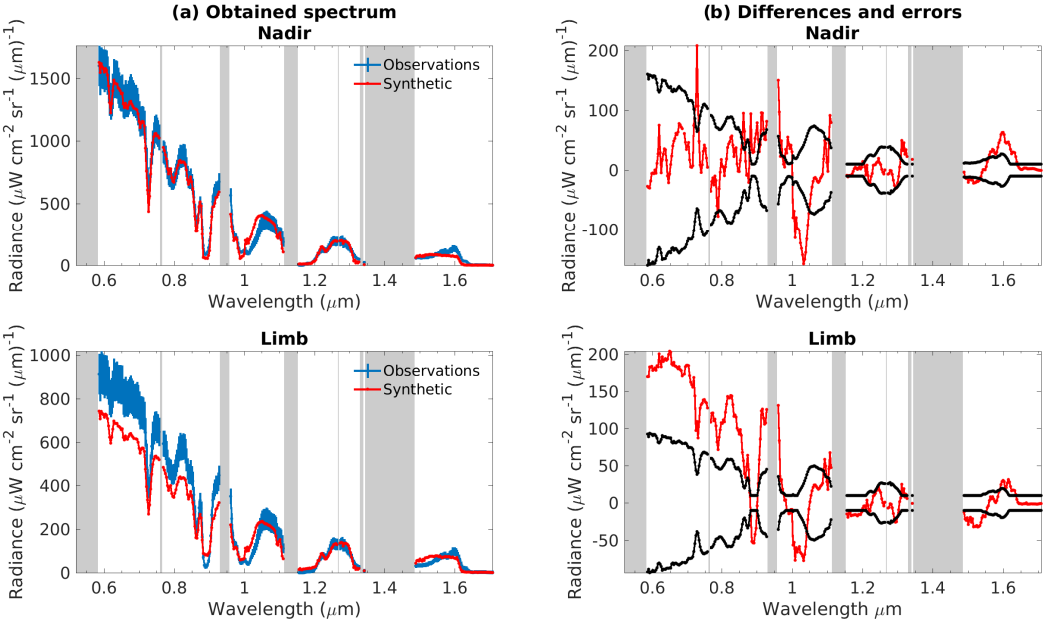

Figure 27: Comparison between observed (blue) and modelled (red) spectra (left column) and comparison between differences (red) and *a priori* errors (black) (right column) for the NEB using model C, with the grey shaded areas corresponding to telluric absorption. The top row corresponds to nadir (incidence and emission angle = 0°) and the bottom row to limb (incidence and emission angle = 61.45°).

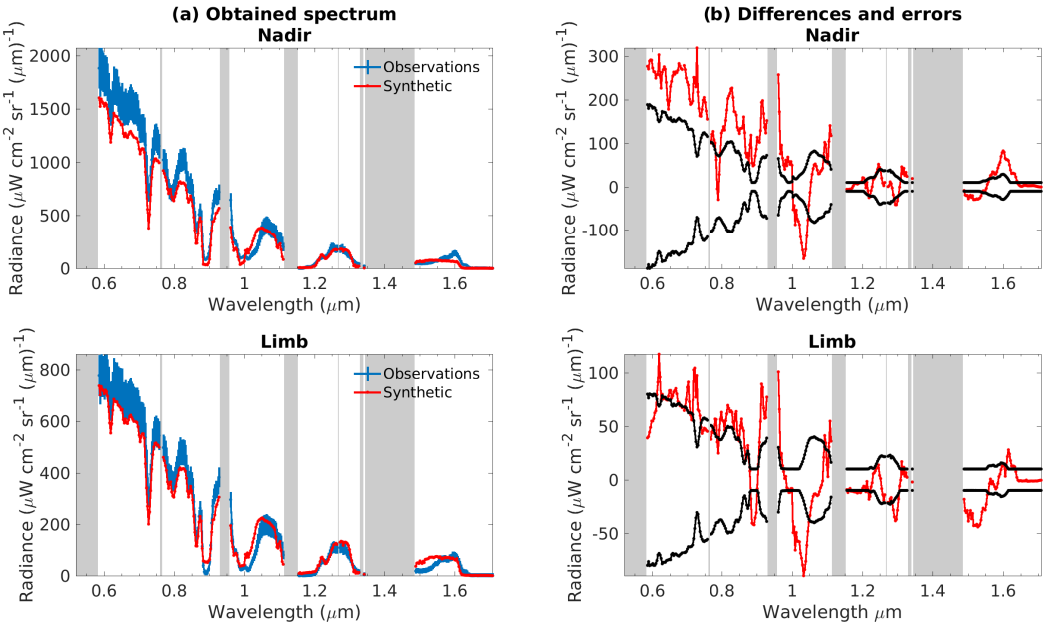

Figure 28: Comparison between observed (blue) and modelled (red) spectra (left column) and comparison between differences (red) and *a priori* errors (black) (right column) for the SEB using model C, with the grey shaded areas corresponding to telluric absorption. The top row corresponds to nadir (incidence and emission angle = 0°) and the bottom row to limb (incidence and emission angle = 61.45°).

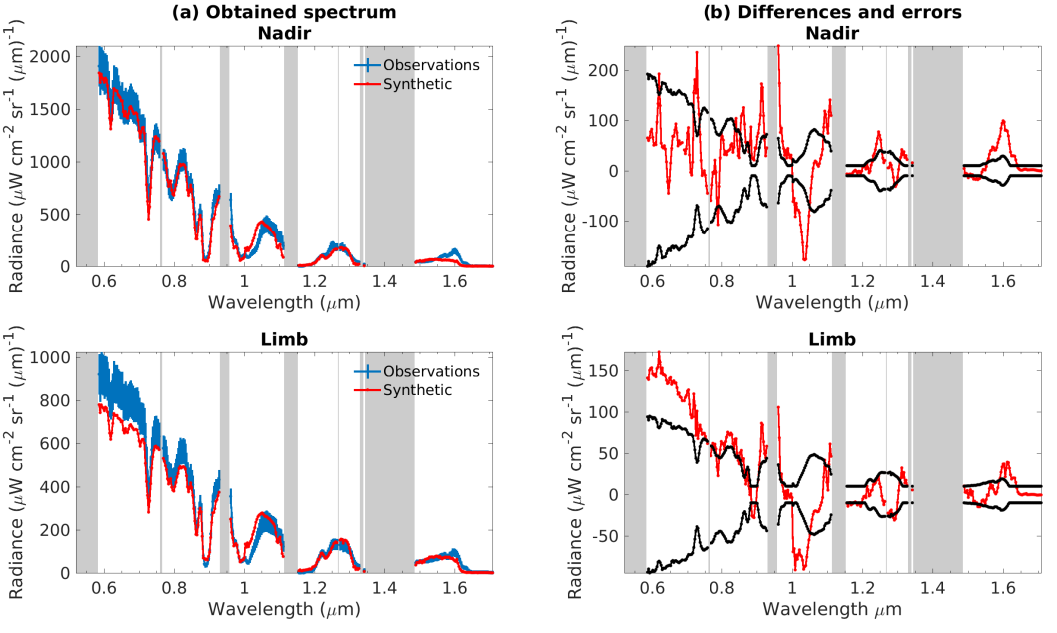

Figure 29: Comparison between observed (blue) and modelled (red) spectra (left column) and comparison between differences (red) and *a priori* errors (black) (right column) for the SEB transition using model C, with the grey shaded areas corresponding to telluric absorption. The top row corresponds to nadir (incidence and emission angle = 0°) and the bottom row to limb (incidence and emission angle = 61.45°).

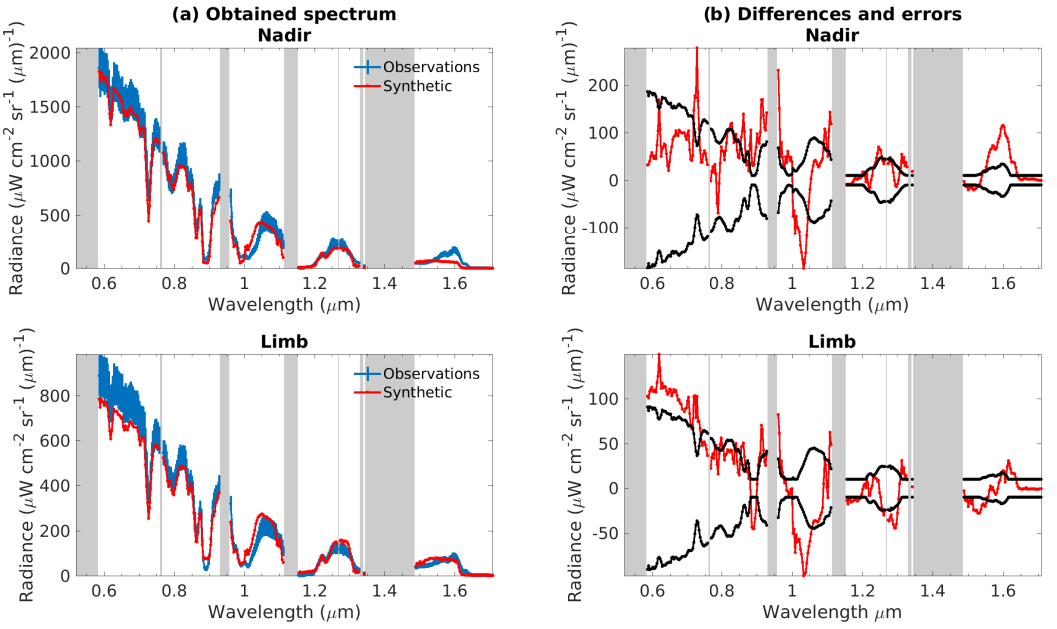

Figure 30: Comparison between observed (blue) and modelled (red) spectra (left column) and comparison between differences (red) and *a priori* errors (black) (right column) for the NEB transition using model C, with the grey shaded areas corresponding to telluric absorption. The top row corresponds to nadir (incidence and emission angle = 0°) and the bottom row to limb (incidence and emission angle = 61.45°).

B. Sensitivity plots and tables

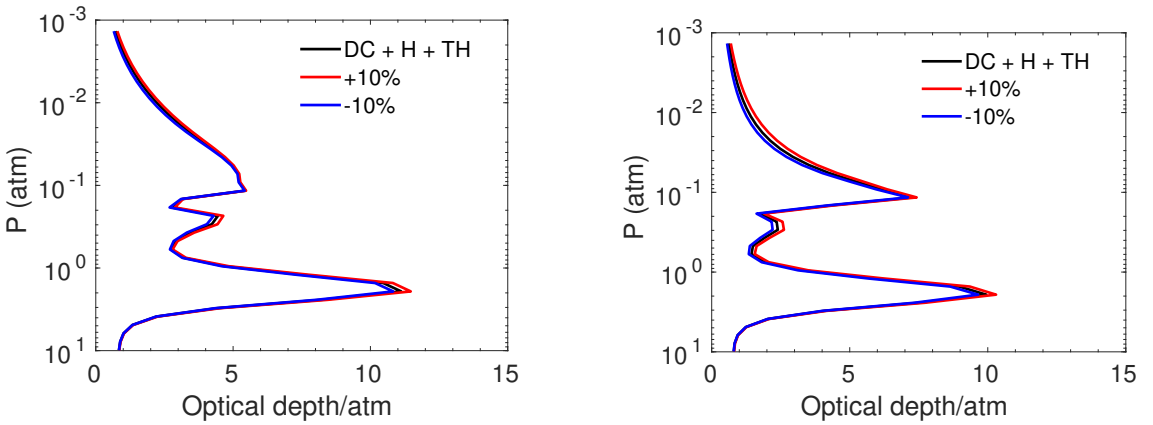

Figure 31: Bracketing analysis of aerosol abundance profiles of the haze and the deep cloud for the EZ (left) and SEB (right). In black we have the obtained vertical profile as shown in Figure 16 (b), in red the resulting vertical profile when the initial vertical abundance profiles of the haze and deep cloud are increased by 10 % and in blue when the same parameters are decreased by 10 %. The optical depth/atm profiles were calculated at 0.89 μm.

Table 10
Obtained χ^2/N_{free} values for the bracketing analysis of models A, B and C for the EZ and SEB regions.

Model	Region	Case	χ^2/N_{free}
Model A	EZ	Nominal	2.04
		Stratospheric haze cloud base abundance +10	2.06
		Stratospheric haze cloud base abundance -10 %	2.02
		Stratospheric haze particle size +10 %	2.10
		Stratospheric haze particle size -10 %	2.12
		Tropospheric haze cloud base abundance +10 %	2.17
		Tropospheric haze cloud base abundance -10 %	2.15
	SEB	Nominal	4.97
		Stratospheric haze cloud base abundance +10 %	1.76
		Stratospheric haze cloud base abundance -10 %	5.36
		Stratospheric haze particle size +10 %	9.72
		Stratospheric haze particle size -10 %	5.21
		Tropospheric haze cloud base abundance +10 %	4.48
		Tropospheric haze cloud base abundance -10 %	1.99
Model B	EZ	Nominal	1.81
		Haze particle size +10 %	1.81
		Haze particle size -10 %	1.81
		Aerosol abundance profile +10 %	1.82
		Aerosol abundance profile -10 %	1.81
	SEB	Nominal	3.26
		Haze particle size +10 %	3.35
		Haze particle size -10 %	3.13
		Aerosol abundance profile +10 %	3.40
		Aerosol abundance profile -10 %	3.15
Model C	EZ	Nominal	2.43
		Stratospheric haze cloud base abundance +10	2.46
		Stratospheric haze cloud base abundance -10 %	2.44
		Tropospheric cloud base pressure +10 %	2.43
		Tropospheric cloud base pressure -10 %	2.49
		Tropospheric cloud cloud base abundance +10 %	2.43
		Tropospheric cloud cloud base abundance -10 %	2.42
	SEB	Nominal	4.27
		Stratospheric haze cloud base abundance +10	4.28
		Stratospheric haze cloud base abundance -10 %	4.33
		Tropospheric cloud base pressure +10 %	4.49
		Tropospheric cloud base pressure -10 %	4.24
		Tropospheric cloud cloud base abundance +10 %	4.43
		Tropospheric cloud cloud base abundance -10 %	4.31

CRediT authorship contribution statement

José Ribeiro: Conceptualization, Data curation, Formal analysis, Investigation, Methodology, Validation, Visualization, Writing - original draft. **Pedro Machado:** Conceptualization, Data curation, Formal analysis, Investigation, Methodology, Supervision, Validation, Visualization, Writing - original draft. **Santiago Pérez-Hoyos:** Conceptualization, Data curation, Formal analysis, Investigation, Methodology, Supervision, Validation, Visualization, Writing - original draft. **Asier Anguiano-Arteaga:** Data curation, Formal analysis, Investigation, Methodology, Validation, Visualization, Writing - original draft. **Patrick Irwin:** Data curation, Formal analysis, Investigation, Methodology, Validation, Visualization, Software, Writing - original draft.

References

Anguiano-Arteaga, A., Pérez-Hoyos, S., Sánchez-Lavega, A., Sanz-Requena, J.F., Irwin, P.G.J., 2021. Vertical Distribution of Aerosols and Hazes Over Jupiter's Great Red Spot and Its Surroundings in 2016 From HST/WFC3 Imaging. Journal of Geophysical Research: Planets 126, e2021JE006996. URL: https://agupubs.onlinelibrary.wiley.com/doi/abs/10.1029/2021JE006996, doi:https://doi.org/10.1029/2021JE006996, arXiv:https://agupubs.onlinelibrary.wiley.com/doi/pdf/10.1029/2021JE006996. e2021JE006996 2021JE006996.

Anguiano-Arteaga, A., Pérez-Hoyos, S., Sánchez-Lavega, A., Sanz-Requena, J.F., Irwin, P.G.J., 2023. Temporal variations in Vertical Cloud Structure of Jupiter's Great Red Spot, Its Surroundings and Oval BA From HST/WFC3 Imaging. Journal of Geophysical Research: Planets 128, e2022JE007427. URL: https://agupubs.onlinelibrary.wiley.com/doi/abs/10.1029/2022JE007427, doi:https://doi.org/10.1029/2022JE007427, arXiv:https://agupubs.onlinelibrary.wiley.com/doi/pdf/10.1029/2022JE007427. e2022JE007427 2022JE007427.

Atreya, S., Wong, M., Owen, T., Mahaffy, P., Niemann, H., de Pater, I., Drossart, P., Encrenaz, T., 1999. A comparison of the atmospheres of Jupiter and Saturn: deep atmospheric composition, cloud structure, vertical mixing, and origin. Planetary and Space Science 47, 1243–1262. URL: https://www.sciencedirect.com/science/article/pii/S0032063399000471, doi:https://doi.org/10.1016/S0032-0633(99)00047-1.

Atreya, S.K., Wong, M.H., Owen, T.C., Niemann, H.B., Mahaffy, P.R., 1998. Chemistry and Clouds of Jupiter's Atmosphere: A Galileo Perspective. Springer Netherlands, Dordrecht. pp. 249–260. URL: https://doi.org/10.1007/978-94-015-8790-7_21, doi:10.1007/978-94-015-8790-7_21.

Baines, K., Sromovsky, L., Carlson, R., Momary, T., Fry, P., 2019. The visual spectrum of Jupiter's Great Red Spot accurately modeled with aerosols produced by photolyzed ammonia reacting with acetylene. Icarus 330, 217–229. URL: https://www.sciencedirect.com/science/article/pii/S0019103516305474, doi:https://doi.org/10.1016/j.icarus.2019.04.008.

Borysow, A., Borysow, J., Fu, Y., 2000. Semi-empirical Model of Collision-Induced Absorption Spectra of H2–H2 Complexes in the Second Overtone Band of Hydrogen at Temperatures from 50 to 500 K. Icarus 145, 601–608. URL: https://www.sciencedirect.com/science/article/pii/S001910350096384X, doi:https://doi.org/10.1006/icar.2000.6384.

Borysow, A., Frommhold, L., 1989. Collision-induced Infrared Spectra of H 2-He Pairs at Temperatures from 18 to 7000 K. II. Overtone and Hot Bands. Astrophysical Journal 341, 549. doi:10.1086/167515.

Braude, A.S., Irwin, P.G., Orton, G.S., Fletcher, L.N., 2020. Colour and tropospheric cloud structure of Jupiter from MUSE/VLT: Retrieving a universal chromophore. Icarus 338, 113589. URL: https://www.sciencedirect.com/science/article/pii/S0019103519304920, doi:https://doi.org/10.1016/j.icarus.2019.113589.

Carlson, R., Baines, K., Anderson, M., Filacchione, G., Simon, A., 2016. Chromophores from photolyzed ammonia reacting with acetylene: Application to Jupiter's Great Red Spot. Icarus 274, 106–115. URL: https://www.sciencedirect.com/science/article/pii/S0019103516001494, doi:https://doi.org/10.1016/j.icarus.2016.03.008.

Chance, K., Kurucz, R., 2010. An improved high-resolution solar reference spectrum for earth's atmosphere measurements in the ultraviolet, visible, and near infrared. Journal of Quantitative Spectroscopy and Radiative Transfer 111, 1289–1295. URL: https://www.sciencedirect.com/science/article/pii/S0022407310000610, doi:https://doi.org/10.1016/j.jqsrt.2010.01.036. special Issue Dedicated to Laurence S. Rothman on the Occasion of his 70th Birthday.

Clark, R.N., McCord, T.B., 1979. Jupiter and Saturn: Near-infrared spectral albedos. Icarus 40, 180–188. URL: https://www.sciencedirect.com/science/article/pii/0019103579900630, doi:https://doi.org/10.1016/0019-1035(79)90063-0.

Coles, P.A., Ovsyannikov, R.I., Polyansky, O.L., Yurchenko, S.N., Tennyson, J., 2018. Improved potential energy surface and spectral assignments for ammonia in the near-infrared region. Journal of Quantitative Spectroscopy and Radiative Transfer URL: https://api.semanticscholar.org/CorpusID:52840068.

Cuzzi, J., Clark, R., Filacchione, G., French, R., Johnson, R., Marouf, E., Spilker, L., 2009. Ring Particle Composition and Size Distribution. Springer Netherlands, Dordrecht. pp. 459–509. URL: https://doi.org/10.1007/978-1-4020-9217-6_15, doi:10.1007/978-1-4020-9217-6_15.

Dahl, E., Chanover, N., Orton, G., Baines, K., Sinclair, J., Voelz, D., Wijerathna, E., Strycker, P., Irwin, P., 2021. Vertical structure and color of jovian latitudinal cloud bands during the juno era. The Planetary Science Journal 2, 16. doi:10.3847/PSJ/abd400.

Fletcher, L., Orton, G., Teanby, N., Irwin, P., 2009. Phosphine on Jupiter and Saturn from Cassini/CIRS. Icarus 202, 543–564. URL: https://www.sciencedirect.com/science/article/pii/S0019103509001328, doi:https://doi.org/10.1016/j.icarus.2009.03.023.

Gordon, I., Rothman, L., Hargreaves, R., Hashemi, R., Karlovets, E., Skinner, F., Conway, E., Hill, C., Kochanov, R., Tan, Y., Wcisło, P., Finenko, A., Nelson, K., Bernath, P., Birk, M., Boudon, V., Campargue, A., Chance, K., Coustenis, A., Drouin, B., Flaud, J., Gamache, R., Hodges, J., Jacquemart, D., Mlawer, E., Nikitin, A., Perevalov, V., Rotger, M., Tennyson, J., Toon, G., Tran, H., Tyuterev, V., Adkins, E., Baker, A., Barbe, A., Canè, E., Császár, A., Dudaryonok, A., Egorov, O., Fleisher, A., Fleurbaey, H., Foltynowicz, A., Furtenbacher, T., Harrison, J., Hartmann, J., Horneman, V., Huang, X., Karman, T., Karns, J., Kassi, S., Kleiner, I., Kofman, V., Kwabia–Tchana, F., Lavrentieva, N., Lee, T., Long, D., Lukashevskaya, A., Lyulin, O., Makhnev, V., Matt, W., Massie, S., Melosso, M., Mikhailenko, S., Mondelain, D., Müller, H., Naumenko, O., Perrin, A., Polyansky, O., Raddaoui, E., Raston, P., Reed, Z., Rey, M., Richard, C., Tóbiás, R., Sadiek, I., Schwenke, D., Starikova, E., Sung, K., Tamassia, F., Tashkun, S., Vander Auwera, J., Vasilenko, I., Vigasin, A., Villanueva, G., Vispoel, B., Wagner, G., Yachmenev, A., Yurchenko, S., 2022. The HITRAN2020 molecular spectroscopic database. Journal of Quantitative Spectroscopy and Radiative Transfer 277, 107949. URL: https://www.sciencedirect.com/science/article/pii/S0022407321004416, doi:https://doi.org/10.1016/j.jqsrt.2021.107949.

Heng, K., Li, L., 2021. Jupiter as an Exoplanet: Insights from Cassini Phase Curves. The Astrophysical Journal Letters 909, L20. doi:10.3847/2041-8213/abe872, arXiv:2101.09984.

Henyey, L.G., Greenstein, J.L., 1941. Diffuse radiation in the Galaxy. Astrophysical Journal 93, 70–83. doi:10.1086/144246.

Irwin, P., Teanby, N., de Kok, R., Fletcher, L., Howett, C., Tsang, C., Wilson, C., Calcutt, S., Nixon, C., Parrish, P., 2008. The NEMESIS planetary atmosphere radiative transfer and retrieval tool. Journal of Quantitative Spectroscopy and Radiative Transfer 109, 1136–1150. URL: https://www.sciencedirect.com/science/article/pii/S0022407307003378, doi:https://doi.org/10.1016/j.jqsrt.2007.11.006. spectroscopy and Radiative Transfer in Planetary Atmospheres.

Irwin, P., Tice, D., Fletcher, L., Barstow, J., Teanby, N., Orton, G., Davis, G., 2015. Reanalysis of Uranus' cloud scattering properties from IRTF/SpeX observations using a self-consistent scattering cloud retrieval scheme. Icarus 250, 462–476. URL: https://www.sciencedirect.com/science/article/pii/S0019103514007003, doi:https://doi.org/10.1016/j.icarus.2014.12.020.

Irwin, P.G., Bowles, N., Braude, A.S., Garland, R., Calcutt, S., 2018. Analysis of gaseous ammonia (NH3) absorption in the visible spectrum of Jupiter. Icarus 302, 426–436. URL: https://www.sciencedirect.com/science/article/pii/S001910351730547X, doi:https://doi.org/10.1016/j.icarus.2017.11.031.

Irwin, P.G., Dobinson, J., James, A., Toledo, D., Teanby, N.A., Fletcher, L.N., Orton, G.S., Pérez-Hoyos, S., 2021. Latitudinal variation of methane mole fraction above clouds in Neptune's atmosphere from VLT/MUSE-NFM: Limb-darkening reanalysis. Icarus 357, 114277. URL: https://www.sciencedirect.com/science/article/pii/S0019103520305972, doi:https://doi.org/10.1016/j.icarus.2020.114277.

Irwin, P.G.J., 2009. Giant Planets of Our Solar System. doi:10.1007/978-3-540-85158-5.

Irwin, P.G.J., Teanby, N.A., Fletcher, L.N., Toledo, D., Orton, G.S., Wong, M.H., Roman, M.T., Pérez-Hoyos, S., James, A., Dobinson, J., 2022. Hazy Blue Worlds: A Holistic Aerosol Model for Uranus and Neptune, Including Dark Spots. Journal of Geophysical Research: Planets 127. URL: http://dx.doi.org/10.1029/2022JE007189, doi:10.1029/2022je007189.

Karkoschka, E., Tomasko, M.G., 2010. Methane absorption coefficients for the jovian planets from laboratory, Huygens, and HST data. Icarus 205, 674–694. URL: https://www.sciencedirect.com/science/article/pii/S0019103509003078, doi:https://doi.org/10.1016/j.icarus.2009.07.044.

Machado, P., Luz, D., Widemann, T., Lellouch, E., Witasse, O., 2012. Mapping zonal winds at Venus's cloud tops from ground-based Doppler velocimetry. Icarus 221, 248–261. doi:10.1016/j.icarus.2012.07.012.

Machado, P., Widemann, T., Luz, D., Peralta, J., 2014. Wind circulation regimes at Venus' cloud tops: Ground-based Doppler velocimetry using CFHT/ESPaDOnS and comparison with simultaneous cloud tracking measurements using VEx/VIRTIS in February 2011. Icarus 243, 249–263. doi:10.1016/j.icarus.2014.08.030.

Martonchik, J.V., Orton, G.S., Appleby, J.F., 1984. Optical properties of NH3 ice from the far infrared to the near ultraviolet. Appl. Opt. 23, 541–547. URL: https://opg.optica.org/ao/abstract.cfm?URI=ao-23-4-541, doi:10.1364/AO.23.000541.

Matcheva, K.I., Conrath, B.J., Gierasch, P.J., Flasar, F.M., 2005. The cloud structure of the jovian atmosphere as seen by the cassini/cirs experiment. Icarus 179, 432–448. URL: https://www.sciencedirect.com/science/article/pii/S0019103505002435, doi:https://doi.org/10.1016/j.icarus.2005.06.020.

McLean, W., Stam, D.M., Bagnulo, S., Borisov, G., Devogèle, M., Cellino, A., Rivet, J.P., Bendjoya, P., Vernet, D., Paolini, G., Pollacco, D., 2017. A polarimetric investigation of Jupiter: Disk-resolved imaging polarimetry and spectropolarimetry. Astronomy & Astrophysics 601, A142. doi:10.1051/0004-6361/201629314.

Mendikoa, I., Sánchez-Lavega, A., Pérez-Hoyos, S., Hueso, R., Rojas, J.F., López-Santiago, J., 2017. Temporal and spatial variations of the absolute reflectivity of Jupiter and Saturn from 0.38 to 1.7 μm with PlanetCam-UPV/EHU. A&A 607, A72. URL: https://doi.org/10.1051/0004-6361/201731109, doi:10.1051/0004-6361/201731109.

Minnaert, M., 1941. The reciprocity principle in lunar photometry. Astrophysical Journal 93, 403–410. doi:10.1086/144279.

Montañes-Rodriguez, P., Gonzalez-Merino, B., Palle, E., López-Puertas, M., Garcia-Melendo, E., 2015. Jupiter as an exoplanet: Uv to nir transmission spectrum reveals hazes, a na layer, and possibly stratospheric h2o-ice clouds. The Astrophysical Journal 801. doi:10.1088/2041-8205/801/1/L8.

Murgas, F., Castro-González, A., Pallé, E., Pozuelos, F.J., Millholland, S., Foo, O., Korth, J., Marfil, E., Amado, P.J., Caballero, J.A., Christiansen, J.L., Ciardi, D.R., Collins, K.A., Di Sora, M., Fukui, A., Gan, T., Gonzales, E.J., Henning, T., Herrero, E., Isopi, G., Jenkins, J.M., Lillo-Box, J., Lodieu, N., Luque, R., Mallia, F., Morales, J.C., Morello, G., Narita, N., Orell-Miquel, J., Parviainen, H., Pérez-Torres, M., Quirrenbach, A., Reiners, A., Ribas, I., Safonov, B.S., Seager, S., Schwarz, R.P., Schweitzer, A., Schlecker, M., Strakhov, I.A., Vanaverbeke, S., Watanabe, N., Winn, J.N., Zechmeister, M., 2023. Two super-Earths at the edge of the habitable zone of the nearby M dwarf TOI-2095. Astronomy & Astrophysics 677, A182. doi:10.1051/0004-6361/202346692, arXiv:2304.09220.

Niemann, H.B., Atreya, S.K., Carignan, G.R., Donahue, T.M., Haberman, J.A., Harpold, D.N., Hartle, R.E., Hunten, D.M., Kasprzak, W.T., Mahaffy, P.R., Owen, T.C., Spencer, N.W., Way, S.H., 1996. The galileo probe mass spectrometer: Composition of jupiter's atmosphere. Science 272, 846–849. URL: https://www.science.org/doi/abs/10.1126/science.272.5263.846, doi:10.1126/science.272.5263.846, arXiv:https://www.science.org/doi/pdf/10.1126/science.272.5263.846.

Niemann, H.B., Atreya, S.K., Carignan, G.R., Donahue, T.M., Haberman, J.A., Harpold, D.N., Hartle, R.E., Hunten, D.M., Kasprzak, W.T., Mahaffy, P.R., Owen, T.C., Way, S.H., 1998. The composition of the Jovian atmosphere as determined by the Galileo probe mass spectrometer. Journal of Geophysical Research: Planets 103, 22831–22845. URL: https://agupubs.onlinelibrary.wiley.com/doi/abs/10.1029/98JE01050, doi:https://doi.org/10.1029/98JE01050, arXiv:https://agupubs.onlinelibrary.wiley.com/doi/pdf/10.1029/98JE01050.

Nowak, G., Luque, R., Parviainen, H., Pallé, E., Molaverdikhani, K., Béjar, V.J.S., Lillo-Box, J., Rodríguez-López, C., Caballero, J.A., Zechmeister, M., Passegger, V.M., Cifuentes, C., Schweitzer, A., Narita, N., Cale, B., Espinoza, N., Murgas, F., Hidalgo, D., Zapatero Osorio, M.R., Pozuelos, F.J., Aceituno, F.J., Amado, P.J., Barkaoui, K., Barrado, D., Bauer, F.F., Benkhaldoun, Z., Caldwell, D.A., Casasayas Barris, N., Chaturvedi, P., Chen, G., Collins, K.A., Collins, K.I., Cortés-Contreras, M., Crossfield, I.J.M., de León, J.P., Díez Alonso, E., Dreizler, S., El Mufti, M., Esparza-Borges, E., Essack, Z., Fukui, A., Gaidos, E., Gillon, M., Gonzales, E.J., Guerra, P., Hatzes, A., Henning, T., Herrero, E., Hesse, K., Hirano, T., Howell, S.B., Jeffers, S.V., Jehin, E., Jenkins, J.M., Kaminski, A., Kemmer, J., Kielkopf, J.F., Kossakowski, D., Kotani, T., Kürster, M., Lafarga, M., Latham, D.W., Law, N., Lissauer, J.J., Lodieu, N., Madrigal-Aguado, A., Mann, A.W., Massey, B., Matson, R.A., Matthews, E., Montañés-Rodríguez, P., Montes, D., Morales, J.C., Mori, M., Nagel, E., Oshagh, M., Pedraz, S., Plavchan, P., Pollacco, D., Quirrenbach,

A., Reffert, S., Reiners, A., Ribas, I., Ricker, G.R., Rose, M.E., Schlecker, M., Schlieder, J.E., Seager, S., Stangret, M., Stock, S., Tamura, M., Tanner, A., Teske, J., Trifonov, T., Twicken, J.D., Vanderspek, R., Watanabe, D., Wittrock, J., Ziegler, C., Zohrabi, F., 2020. The CARMENES search for exoplanets around M dwarfs. Two planets on opposite sides of the radius gap transiting the nearby M dwarf LTT 3780. Astronomy & Astrophysics 642, A173. doi:10.1051/0004-6361/202037867, arXiv:2003.01140.

Pérez-Hoyos, S., Sánchez-Lavega, A., Sanz-Requena, J., Barrado-Izagirre, N., Carrión-González, O., Anguiano-Arteaga, A., Irwin, P., Braude, A., 2020. Color and aerosol changes in Jupiter after a North Temperate Belt disturbance. Icarus 352, 114031. URL: https://www.sciencedirect.com/science/article/pii/S0019103520303900, doi:https://doi.org/10.1016/j.icarus.2020.114031.

Quirrenbach, A., Amado, P.J., Caballero, J.A., Mundt, R., Reiners, A., Ribas, I., Seifert, W., Abril, M., Aceituno, J., Alonso-Floriano, F.J., Anwand-Heerwart, H., Azzaro, M., Bauer, F., Barrado, D., Becerril, S., Bejar, V.J.S., Benitez, D., Berdinas, Z.M., Brinkmöller, M., Cardenas, M.C., Casal, E., Claret, A., Colomé, J., Cortes-Contreras, M., Czesla, S., Doellinger, M., Dreizler, S., Feiz, C., Fernandez, M., Ferro, I.M., Fuhrmeister, B., Galadi, D., Gallardo, I., Gálvez-Ortiz, M.C., Garcia-Piquer, A., Garrido, R., Gesa, L., Galera, V.G., Hernández, J.I.G., Peinado, R.G., Grözinger, U., Guàrdia, J., Guenther, E.W., de Guindos, E., Hagen, H.J., Hatzes, A.P., Hauschildt, P.H., Helmling, J., Henning, T., Hermann, D., Arabi, R.H., Castaño, L.H., Hernando, F.H., Herrero, E., Huber, A., Huber, K.F., Huke, P., Jeffers, S.V., de Juan, E., Kaminski, A., Kehr, M., Kim, M., Klein, R., Klüter, J., Kürster, M., Lafarga, M., Lara, L.M., Lamert, A., Laun, W., Launhardt, R., Lemke, U., Lenzen, R., Llamas, M., del Fresno, M.L., López-Puertas, M., López-Santiago, J., Salas, J.F.L., Madinabeitia, H.M., Mall, U., Mandel, H., Mancini, L., Molina, J.A.M., Fernández, D.M., Martín, E.L., Martín-Ruiz, S., Marvin, C., Mathar, R.J., Mirabet, E., Montes, D., Morales, J.C., Muñoz, R.M., Nagel, E., Naranjo, V., Nowak, G., Palle, E., Panduro, J., Passegger, V.M., Pavlov, A., Pedraz, S., Perez, E., Pérez-Medialdea, D., Perger, M., Pluto, M., Ramón, A., Rebolo, R., Redondo, P., Reffert, S., Reinhart, S., Rhode, P., Rix, H.W., Rodler, F., Rodríguez, E., López, C.R., Rohloff, R.R., Rosich, A., Carrasco, M.A.S., Sanz-Forcada, J., Sarkis, P., Sarmiento, L.F., Schäfer, S., Schiller, J., Schmidt, C., Schmitt, J.H.M.M., Schöfer, P., Schweitzer, A., Shulyak, D., Solano, E., Stahl, O., Storz, C., Tabernero, H.M., Tala, M., Tal-Or, L., Ulbrich, R.G., Veredas, G., Linares, J.I.V., Vilardell, F., Wagner, K., Winkler, J., Osorio, M.R.Z., Zechmeister, M., von Eiff, M.A., Anglada-Escudé, G., del Burgo, C., Garcia-Vargas, M.L., Klutsch, A., Lizon, J.L., Lopez-Morales, M., Ofir, A., Pérez-Calpena, A., Perryman, M.A.C., Sánchez-Blanco, E., Strachan, J.B.P., Stürmer, J., Suárez, J.C., Trifonov, T., Tulloch, S.M., Xu, W., 2016. CARMENES: an overview six months after first light, in: Evans, C.J., Simard, L., Takami, H. (Eds.), Ground-based and Airborne Instrumentation for Astronomy VI, International Society for Optics and Photonics. SPIE. p. 990812. URL: https://doi.org/10.1117/12.2231880, doi:10.1117/12.2231880.

Ragent, B., Colburn, D.S., Rages, K.A., Knight, T.C.D., Avrin, P., Orton, G.S., Yanamandra-Fisher, P.A., Grams, G.W., 1998. The clouds of Jupiter: Results of the Galileo Jupiter Mission Probe Nephelometer Experiment. Journal of Geophysical Research: Planets 103, 22891–22909. URL: https://agupubs.onlinelibrary.wiley.com/doi/abs/10.1029/98JE00353, doi:https://doi.org/10.1029/98JE00353.

Rodgers, C.D., 2000. Inverse Methods for Atmospheric Sounding. WORLD SCIENTIFIC. URL: https://worldscientific.com/doi/abs/10.1142/3171, doi:10.1142/3171, arXiv:https://worldscientific.com/doi/pdf/10.1142/3171.

Seiff, A., Kirk, D.B., Knight, T.C.D., Young, R.E., Mihalov, J.D., Young, L.A., Milos, F.S., Schubert, G., Blanchard, R.C., Atkinson, D., 1998. Thermal structure of Jupiter's atmosphere near the edge of a 5-μm hot spot in the north equatorial belt. Journal of Geophysical Research: Planets 103, 22857–22889. URL: https://agupubs.onlinelibrary.wiley.com/doi/abs/10.1029/98JE01766, doi:https://doi.org/10.1029/98JE01766, arXiv:https://agupubs.onlinelibrary.wiley.com/doi/pdf/10.1029/98JE01766.

Sromovsky, L., Baines, K., Fry, P., Carlson, R., 2017. A possibly universal red chromophore for modeling color variations on Jupiter. Icarus 291, 232–244. URL: https://www.sciencedirect.com/science/article/pii/S0019103516303700, doi:https://doi.org/10.1016/j.icarus.2016.12.014.

Sromovsky, L., Fry, P., 2002. Jupiter's cloud structure as constrained by galileo probe and hst observations. Icarus 157, 373–400. URL: https://www.sciencedirect.com/science/article/pii/S0019103502968442, doi:https://doi.org/10.1006/icar.2002.6844.

Stoll, C.P., 1980. Polarimetry of Jupiter at large phase angles (Ph.D. thesis). The University of Arizona.

Taylor, F.W., Atreya, S.K., Encrenaz, T., Hunten, D.M., Irwin, P.G.J., Owen, T.C., 2004. The composition of the atmosphere of Jupiter, in: Bagenal, F., Dowling, T.E., McKinnon, W.B. (Eds.), Jupiter. The Planet, Satellites and Magnetosphere. volume 1, pp. 59–78.

Villanueva, G.L., Smith, M.D., Protopapa, S., Faggi, S., Mandell, A.M., 2018. Planetary Spectrum Generator: An accurate online radiative transfer suite for atmospheres, comets, small bodies and exoplanets. Journal of Quantitative Spectroscopy and Radiative Transfer 217, 86–104. doi:10.1016/j.jqsrt.2018.05.023, arXiv:1803.02008.

West, R.A., Baines, K.H., Friedson, A.J., Banfield, D., Ragent, B., Taylor, F.W., 2004. Jovian clouds and haze. Jupiter: The planet, satellites and magnetosphere 79, 104.

von Zahn, U., Hunten, D.M., Lehmacher, G., 1998. Helium in Jupiter's atmosphere: Results from the Galileo probe helium interferometer experiment. Journal of Geophysical Research: Planets 103, 22815–22829. URL: https://agupubs.onlinelibrary.wiley.com/doi/abs/10.1029/98JE00695, doi:https://doi.org/10.1029/98JE00695, arXiv:https://agupubs.onlinelibrary.wiley.com/doi/pdf/10.1029/98JE00695.

Zhang, X., West, R., Banfield, D., Yung, Y., 2013. Stratospheric aerosols on Jupiter from Cassini observations. Icarus 226, 159–171. URL: https://www.sciencedirect.com/science/article/pii/S0019103513002200, doi:https://doi.org/10.1016/j.icarus.2013.05.020.

Zhang, X., West, R.A., Irwin, P.G.J., Nixon, C.A., Yung, Y.L., 2015. Aerosol influence on energy balance of the middle atmosphere of Jupiter. Nature Communications 6, 10231. doi:10.1038/ncomms10231.